

Assessing the photometric redshift precision of the S-PLUS survey: the Stripe-82 as a test-case.

A. Molino^{1*}, M. V. Costa-Duarte¹, L. Sampedro¹, F. R. Herpich¹, L. Sodré Jr.¹, C. Mendes de Oliveira¹, W. Schoenell², C. E. Barbosa¹, C. Queiroz³, E. V. R. Lima¹, L. Azanha¹, N. Muñoz-Elgueta^{4,5}, T. Ribeiro⁶, A. Kanaan⁷, J. A. Hernandez-Jimenez^{8,1}, A. Cortesi⁹, S. Akras^{10,11}, R. Lopes de Oliveira^{12,11,13}, S. Torres-Flores⁴, C. Lima-Dias⁴, J. L. Nilo Castellon⁴, G. Damke^{4,5}, A. Alvarez-Candal¹¹, Y. Jiménez-Teja¹¹, P. Coelho¹, E. Pereira¹⁴, A. D. Montero-Dorta¹⁵, N. Benítez¹⁶, T. S. Gonçalves⁸, L. Santana-Silva⁸, S. V. Werner¹, L. A. Almeida^{17,1}, P. A. A. Lopes⁸, A. L. Chies-Santos², E. Telles¹⁰, Thom de Souza, R. C.¹⁹, D. R. Gonçalves⁸, R. S. de Souza¹⁸, M. Makler²⁰, V. M. Placco^{21,22}, L. M. I. Nakazono¹, R. K. Saito⁷, R. A. Overzier^{11,1}, L. R. Abramo³

Affiliations can be found after the references.

Submitted to MNRAS.

ABSTRACT

In this paper we present a thorough discussion about the photometric redshift (photo- z) performance of the Southern Photometric Local Universe Survey (S-PLUS). This survey combines a 7 narrow + 5 broad passband filter system, with a typical photometric-depth of $r \sim 21$ AB. For this exercise, we utilize the Data Release 1 (DR1), corresponding to 336 deg^2 from the Stripe-82 region. We rely on the BPZ2 code to compute our estimates, using a new library of SED models, which includes additional templates for quiescent galaxies. When compared to a spectroscopic redshift control sample of $\sim 100\text{k}$ galaxies, we find a precision of $\sigma_z < 0.8\%$, $< 2.0\%$ or $< 3.0\%$ for galaxies with magnitudes $r < 17$, < 19 and < 21 , respectively. A precision of 0.6% is attained for galaxies with the highest Odds values. These estimates have a negligible bias and a fraction of catastrophic outliers inferior to 1% . We identify a redshift window (i.e., $0.26 < z < 0.32$) where our estimates double their precision, due to the simultaneous detection of two emission-lines in two distinct narrow-bands; representing a window opportunity to conduct statistical studies such as luminosity functions. We forecast a total of $\sim 2\text{M}$, $\sim 16\text{M}$ and $\sim 32\text{M}$ galaxies in the S-PLUS survey with a photo- z precision of $\sigma_z < 1.0\%$, $< 2.0\%$ and $< 2.5\%$ after observing 8000 deg^2 . We also derive redshift Probability Density Functions, proving their reliability encoding redshift uncertainties and their potential recovering the $n(z)$ of galaxies at $z < 0.4$, with an unprecedented precision for a photometric survey in the southern hemisphere.

Key words: cosmology: large-scale structure of Universe – galaxies: distances and redshifts – galaxies: photometry – galaxies: clusters: general – surveys

1 INTRODUCTION

Modern astronomy has entered a new era of massive data acquisition. The current and new generation of redshift surveys such as the Sloan Digital Sky Survey (SDSS; York

et al. 2000), Pan-STARRS Kaiser et al. 2002, the Dark Energy Survey (DES; Drlica-Wagner et al. 2018), the Large Synoptic Survey Telescope (LSST; Ivezić et al. 2008), the Baryon Oscillation Spectroscopic survey (BOSS; Schlegel et al. 2009), EUCLID Refregier et al. 2010, the Dark Energy Spectroscopic Instrument (DESI; Levi et al. 2013) and the Javalambre-Physics of the Accelerated Universe Astronomical survey (J-PAS; Benítez et al. 2009a, Benítez et al.

* E-mail: albertomolino.work@gmail.com

2014) among others, will provide either multicolor or spectral information for millions of galaxies, enabling precise cosmological studies at different cosmic epochs.

In this context, photometric redshifts (photo-z) have become an essential tool in modern astronomy since they represent a quick and relatively inexpensive way of retrieving redshift estimates for a large amount of galaxies in a reasonable amount of observational time. In the last few decades, photometric redshift surveys have been mainly undertaken the following two pathways: higher wavelength resolution and moderate depth using medium-to-narrow filters versus deeper observations with poor resolution using standard broadband filters. The strong dependency between the wavelength resolution (number and type of passbands) and the achievable precision of photo-z estimates (Hickson et al. 1994, Hickson & Mulrooney 1998, Wolf et al. 2001, Benítez et al. 2009b) has inspired the design of a whole generation of medium-to-narrow multi-band photometric redshift surveys such as the Classifying Object by Medium-Band Observations-17 survey (COMBO-17; Wolf et al. (2003)), the Multiwavelength Survey by Yale-Chile (MUSYC; Gawiser et al. (2006)), the Advance Large Homogeneous Medium Band Redshift Astronomical survey (ALHAMBRA; Moles et al. (2008)), the Cluster Lensing and Supernovae with Hubble survey (CLASH; Postman et al. (2012)) and the Survey for High-z Absorption Red and Dead Sources (SHARDS; Pérez-González et al. (2013)) among others, reaching photo-z estimates as accurate as $\Delta z/(1+z) < 0.01$ for high signal-to-noise ratio (S/N) galaxies. If we take into account that the new generation of multi narrow-band photometric surveys will surpass the photometric-depth of current spectroscopic redshift surveys such as SDSS ($r < 18$, Alam et al. (2015)) and will provide increasingly more accurate photometric redshift estimations, it is expected that the current picture of the physical processes governing the assembling history and evolution of the Universe that we have today will be soon rebuilt. Meanwhile, very deep broadband photometric observations such as the Hubble Deep Field (HDF; Ferguson et al. (1995)), the Hubble Ultra-Deep Field (HUDF; Beckwith et al. (2006)), the Cosmic Assembly Near-infrared Deep Extragalactic Legacy Survey (CANDELS; Grogin et al. (2011)), the Hubble Extreme Deep Field (XDF; Illingworth et al. (2013)), the Hubble Frontiers Field program (HFF; Lotz et al. (2017)) or the REionization Lensing Cluster Survey (RELICS; ?) among others, even with a limited photo-z accuracy of $\Delta z/(1+z) > 0.05$, have extended our current knowledge on the formation and evolution of galaxies all the way back to a $z \sim 10-12$.

The Southern-Photometric Local Universe Survey (S-PLUS¹; Mendes de Oliveira et al., (subm.)) is an on-going observational program aiming at imaging 9300 deg² from the Southern Hemisphere, with a 0.8 m and 1.4 x 1.4 deg² Field-of-View robotic telescope (hereafter T80S). The S-PLUS is equipped with an optical filter system (Figure 1) designed to perform accurate photometric stellar spectral-type classifications (Bailer-Jones (2004), Jordi et al. (2006), Marín-Franch et al. (2012), Gruel et al. (2012)). The system covers

the entire optical range, from 3700Å to 9000Å, with a total of 12 photometric bands. In particular, the system includes 5 standard broad-bands (u, g, r, i & z) useful to constrain the spectral continuum of the sources and 7 narrow ($\sim 150\text{Å}$ -width) bands (J0378, J0395, J0410, J0430, J0515, J0660, J0861) to trace the [OIII], Ca H+k, H δ , G-band, Mgb Triplet, H α and Ca Triplet features, respectively. Although the filter system was originally designed for the star classification, its wavelength resolution renders possible to attain accurate distance estimates for nearby and low-redshift galaxies and for galaxies at specific redshift windows (see Section 3 of this paper for a thorough discussion). Filter transmission curves for the S-PLUS survey can be accessed through its website². Along with this filter system, T80S is equipped with an optical imager composed of a 9k x 9k pixel-array and a 0.55/pixel scale (see Marin-Franch et al. (2015), Cenarro et al. (2019), Mendes de Oliveira et al., (subm.)), for more details). The combination of all these three elements (e.g., accurate photo-z estimates for nearby galaxies, a wide Field-of-View and a detector with a large pixel-array) makes S-PLUS a powerful dataset to carry out systematic IFU-like analysis for all spatially resolved galaxies, eliminating biases due to preselected samples.

The S-PLUS project will simultaneously conduct several sub-surveys, in most cases using different observational strategies, aiming at tackling different scientific cases. Here we briefly summarize the main characteristic and scientific goals of the **Main Survey** (hereafter MS) and we refer the interested reader to Mendes de Oliveira et al., (subm.) for an in-depth description of these observational programs. The MS is motivated to conduct extragalactic science. The superb photometric redshift estimations provided by the S-PLUS survey in the nearby Universe (see Section 3) will allow to complement current analysis of the large-scale structure of the Universe, without relying on bright colour-based pre-selected spectroscopic galaxy samples. The footprint has been designed to have large overlapping areas with already existing or forthcoming deep extra-galactic surveys such as DES, KiDS, ATLAS and LSST. These common regions will serve both for calibration purposes of the S-PLUS observations and to provide improved photometric redshifts for objects in these fields down to $i=21$ magnitudes.

The superb precision of the S-PLUS photometric redshift in the nearby Universe, compared to similar 4-5 pass-band photometric redshift surveys of similar depth (see Molino et al. 2019 for a detailed discussion), will make possible to revisit fundamental aspects of extragalactic astronomy, such as the formation of the structures in the Universe at (i.e., groups or clusters of galaxies) and the large-scale structure of the nearby Universe at the present epoch, due to the large observational surveyed area (i.e., 8000 deg²). The data and results presented in this work correspond to those obtained from the Data Release I (DR1) of the MS. This means that the precision achieved by the S-PLUS photometric redshifts might not necessarily correspond to the one achievable using the data from another sub-survey, where the number of filters and/or the photometric-depth of the observations may vary substantially.

¹ <http://www.splus.iag.usp.br>

² <http://www.splus.iag.usp.br/en/camera-and-filters/>

This paper is organized as follows. Section 2 opens this paper with a description of the dataset utilized in this exercise. In Section 3, we introduce the photometric redshift code chosen for this work, the new updates that were required to fulfill the specifications of the S-PLUS survey, the evaluation matrices and the discussion of the precision achieved. Along with this, this section also includes a comparison with other catalogues, a discussion about the role of narrow-band filters and the identification of a redshift window where our estimates get boosted due to a simultaneous detection of emission lines. Section 4 motivates the computation of Probability Density Functions and presents a number of statistical tests to prove its reliability. Section 5 explains how the absolute magnitude and the stellar mass content is calculated along with a quantification about how uncertainties in redshift propagate into these estimates. Section 6 is devoted to the characterization of the quality of input the multi-band photometric data. This exercise includes a check-up of the photometric zero-points and validation of the photometric uncertainties. Final Sections, i.e., 7, 8, 9 include, respectively, a list of directions about how to use and access the data along with a number of tables detailing the performance of our photometric redshift estimates.

Unless specified otherwise, all magnitudes here are presented in the AB system. Throughout this work, we have adopted the cosmological model provided by the Planck Collaboration et al. (2014) with parameters $(h_0, \Omega_M, \Omega_\Lambda, \Omega_K) = (0.70, 0.31, 0.69, 0.00)$.

2 DATA

Through the following subsections, we describe the data utilized in this work. Initially, in Section 2.1, we describe our observations in terms of area and depth. Then, in Section 2.2, we briefly review both the S-PLUS image-reduction and calibration pipeline and the main aspects of our photometric pipeline. Section 2.3 summarizes the available public data in the Stripe-82 from other surveys or facilities. Finally, in Section 2.4, we describe the spectroscopic redshift galaxy sample selected for the characterization of our photometric redshift estimations.

2.1 Observations

We choose the Stripe-82 region to characterize the expected precision of the S-PLUS photometric redshifts. The area, which is a 2.5 degree wide and 270 degree long stripe along the Celestial Equator in the Southern Galactic Cap (i.e., $-50^\circ < \alpha < 59^\circ$, $-1.25^\circ < \delta < 1.25^\circ$), has been extensively observed by a large number of facilities (see Section 2.3), counting with abundant public spectroscopic redshift information for a large number of galaxies, down to a magnitude $r=22$. Therefore, it is ideal for data verification purposes.

In this work, we make use of the S-PLUS Data Release 1 (DR1), which corresponds to a total area of 336 deg^2 across the Stripe-82 region, divided in a total of 170 individual and contiguous pointings. The observations were gathered during two periods: from August to November, 2016 and from August to October 2018, as part of the Main Survey

(MS) (see Mendes de Oliveira et al. (subm.) for further information). Every pointing is observed with our 12-band filter system (see Figure 1). As described in Sampedro et al., (in prep.), the MS observations reach a typical photometric-depth of $r \sim 21$ magnitudes in the 5 broad-bands and $r \sim 20.5$ magnitudes in the 7 narrow-bands, for sources detected with a significance larger than $S/N > 3$. Since these observations also correspond to S-PLUS verification data, it is expected a certain level of inhomogeneity in the data in terms of depth, due to an unequal amount of co-added images. Although the Stripe-82 regions do not contain very bright stars, several of the DR1 images do present saturated stars due to the integration time requested for the MS. Since a masking of saturated stars was not applied to our images, photometry for detections near saturated stars might be compromised. Although accurate photometry for bright stars (i.e., $r < 12$) is performed in the Ultra-Short survey (USS), we do not make use of that information, restricting the data to the specification of the MS.

2.2 Photometric Catalogues.

In this section we revise the procedure adopted in S-PLUS to produce the photometric catalogues used in this work. We refer the interested reader to Cenarro et al. (2019) or to Mendes de Oliveira et al., (subm.) for a further discussion on the data-reduction process, and to Sampedro et al., (in prep.) for a thorough discussion on the photometric calibration and photometry extraction.

In short, raw individual images are reduced on a daily-basis following a standard procedure (i.e., bias, flat-field and fringing subtraction), where cold and hot pixels, cosmic rays and satellite tracks are detected and masked out. Final PSF-homogenized and astrometriced co-added science images are generated as a combination of individual exposures from each filter using, respectively, SExtractor (Bertin & Arnouts 2010) and PSFEx (Bertin 2013), SCAMP (Bertin 2010a) and SWARP (Bertin 2010b) software.

Photometric calibration is carried out in a two-step process. A relative calibration is first computed using a new technique presented in Sampedro et al. (in prep.), specifically developed for wide-field multi-band photometric surveys such as S-PLUS, J-PLUS (Cenarro et al. 2019), J-PAS (Benítez et al. 2014) and LSST (Ivezic et al. 2008). This technique utilizes already available multi-band photometric catalogues from other surveys, such as SDSS (see Ivezić et al. 2007; Padmanabhan et al. 2008), Pan-STARRS (Schlafly et al. 2012), DES (see Drlica-Wagner et al. 2018; Burke et al. 2018) and KiDS (de Jong et al. 2015), to predict the colours of main sequence stars in the S-PLUS filter system. Finally, a homogeneous absolute calibration is performed bringing the S-PLUS photometry to that from Gaia (Arenou et al. 2017). As demonstrated in Sampedro et al., (in prep.), this technique is capable to provide zero-point estimates with uncertainties around 2-3%, without needing to rely on long observational campaigns to observed standard stars in every filter and pointing.

The S-PLUS photometric pipeline produces aperture-matched PSF-corrected multi-band photometric catalogues for every field. This pipeline is similar to those presented

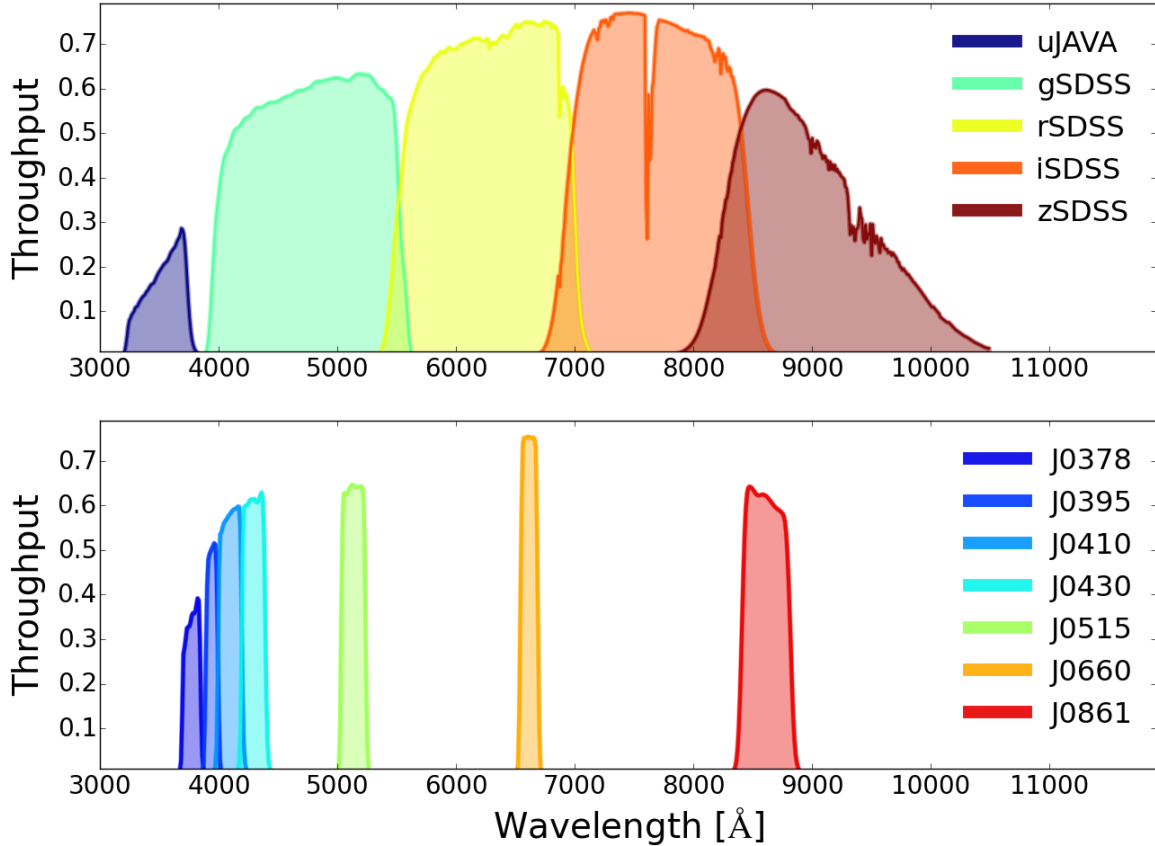


Figure 1. The S-PLUS filter system. Top and bottom panels show, respectively, the 5 broad- and 7 narrow-band filters.

in other surveys such as the ALHAMBRA survey (Molino et al. 2014), the CLASH survey (Molino et al. 2017) or the J-PLUS survey (Molino et al. 2019). This photometric pipeline, which is based on the **SExtractor** software, provides different photometries defined in various types of apertures to accommodate a large number of scientific cases. Sources identified on detection images, combination of the reddest (griz) broad-band images. Photometric uncertainties, initially derived by **SExtractor** software, are re-computed on an image-by-image basis, to account for the correlation among adjacent pixels introduced during the image-reduction and co-adding process. These re-estimations serve to both to improve posterior SED-fitting analysis (i.e., setting realistic uncertainties) and to provide more reliable photometric upper-limits. In this paper, we have relied on the most restricted apertures derived in S-PLUS (i.e., `auto_restricted`) to compute photometric redshifts, since these apertures provide accurate colours and high signal-to-noise magnitudes (Molino et al. 2017).

2.3 The Stripe-82: archival data.

The Stripe-82 is a 2.5 degree wide and 270 degree long stripe along the Celestial Equator in the Southern Galactic Cap

(i.e., $-50^\circ < \alpha < 59^\circ$, $-1.25^\circ < \delta < 1.25^\circ$), extensively observed by a large number of facilities, covering a wide range in wavelength. In the following sections, we summarize the different photometric and spectroscopic programs which have performed observations over this area, providing basic information and references.

2.3.1 Imaging data.

As part of the Data Release 7 (SDSS/DR7; Abazajian et al. 2009) and as part of the SDSS/Supernovae Survey (Frieman et al. 2008), the Sloan Digital Sky Survey has repeatedly scanned the Stripe-82 region, reaching an imaging depth two magnitudes deeper than the main SDSS survey (Annis et al. 2014; Jiang et al. 2014; Fliri & Trujillo 2016). In addition to the SDSS imaging, this region has been observed in the optical wavelength range by other programs such as the CFTH/MegaCam Stripe-82 Survey (CS82; Erben et al. 2013) and the Dark Energy Survey (DES; The Dark Energy Survey Collaboration et al. 2017). At other wavelengths, the Stripe-82 has been covered by GALEX in the far- and near-UV (Morrissey et al. 2007), by the United Kingdom Infrared Deep Sky Survey (UKIDSS; Lawrence et al. 2007), the VISTA/CFHT Stripe 82 Near-infrared Sur-

vey (Geach et al. 2017) and the UKIDSS Deep eXtragalactic Survey (DXS; Lawrence et al. 2007) in the NIR, by the Wide-field Infrared Survey Explorer (WISE; Wright et al. 2010), the Spitzer HETDEX Exploratory Large-area Survey (SHELA, Papovich et al. 2016) and the Spitzer IRAC Equatorial Survey (SpIES, Timlin et al. 2016) in the MIR. At longer wavelengths, in the FIR, the Herschel Stripe 82 Survey (HerS; Viero et al. 2014), and the HerMES Large Mode Survey (HeLMS; Asboth et al. 2016). In the microwaves, the Atacama Cosmology Telescope (ACT; Fowler et al. 2010) and the Very Large Array (VLA; Hodge et al. 2011; Heywood et al. 2016). In Radio wavelengths, the Caltech-NRAO Stripe 82 Survey (CNSS; Mooley et al. 2016). Finally, in the X-rays domain, the Stripe-82 has also been covered by Chandra and XMM-Newton (Franzen et al. 2014; LaMassa et al. 2016).

2.3.2 Spectroscopic redshifts.

Along with the imaging data presented in the previous section, the Stripe-82 already has a large number of spectra, with tens of thousands of redshift measurements from SDSS (Abolfathi et al. 2018), 2SLAQ (Richards et al. 2005), 2dF (Colless et al. 2001), 6dF (Jones et al. 2004), DEEP2 (Newman et al. 2013), VVDS (Le Fèvre et al. 2005), and PRIMUS (Coil et al. 2011), SDSS-III Baryon Oscillation Spectroscopic Survey (BOSS; Dawson et al. 2013), SDSS-IV/eBOSS (Albareti et al. 2017) and WiggleZ (Drinkwater et al. 2010). Further details about the photometric properties (i.e., colours and depths) of these spectroscopic redshift samples can be found in Section 3.2 of Soo et al. (2018).

2.4 The spectroscopic control sample.

In order to characterize the precision and reliability of our photometric redshift estimations, we have compiled a sample of $\sim 100k$ galaxies with known spectroscopic redshifts. As explained in Section 3, in this work we are using the BPZ2 code with a library of regular galaxy models (i.e., neither AGN nor QSO models included) to compute our photometric redshifts³. In order to decontaminate the original compilation of galaxies from AGNs and QSOs, we made the following exercise. First, we ran the BPZ2 code using the ONLY_TYPE = YES mode, to redshift all galaxy models in its library to the corresponding spectroscopic redshift value. Based on the S-PLUS photometry for each galaxy, the BPZ2 code searches for the model that minimizes the differences between data and models. Finally, all sources with very poor fitting (i.e, very high χ^2 values) are discarded since these sources may correspond either to AGN or QSOs, poor-photometry sources, mismatched sources, variable sources or galaxies with extreme colours. It is worth stressing that although this selection may exclude some real galaxies from the analysis, it serves to eliminate potential contaminants that are not the main goal of this paper which is to characterize the real performance of the S-PLUS survey for regular galaxies.

³ The precision for QSO and AGNs will be estimated in two separate papers: Queiroz et al., (in prep.) and Nakazono et al., (in prep.).

As stressed in Mendes de Oliveria et al., (subm.) or in Cenarro et al. (2019), one of the main advantages of using photometric redshift surveys, such as S-PLUS and J-PLUS, instead of spectroscopic redshift samples in the study of the nearby universe, is that the former ones present a larger completeness and homogeneity in their samples since they do not depend on any previously selected sample. In terms of the characterization of the expected performance of a photometric redshift survey, this effect needs to be considered since the availability of complete spectroscopic surveys down to faint magnitudes is very scarce. Therefore, results from deep photometric redshift surveys for the faintest magnitude bins have to be interpreted with care since spectroscopic samples (used for the validation) tend to be dominated by selection effects. Fortunately, for the specific case of this work, this situation has a marginal impact. One reason for choosing the Stripe-82 for the validation of our photometric redshifts, was that this region has spectroscopic redshift information for a large fraction of relatively faint galaxies (i.e., $r > 20$). This means that the S-PLUS observations are similar in terms of depth and colour-coverage to those provided by the compiled spectroscopic sample.

To prove this statement, we have compared the colour, magnitude, redshift and spectral-type distribution of both photometric and spectroscopic samples. On the top left panel of Figure 2, we have represented a colour-colour distribution (i.e., $g-r$ versus $r-i$) of both samples. In order to facilitate its visualization, the number density of sources from the spectroscopic sample (a.k.a., “spectroscopy”) represented with red contours whereas the photometric sample (a.k.a., “S-PLUS/photometry”) has been colour-coded using circular markers. As seen from this panel, both samples present a very similar distribution in this colour-colour space. Interestingly, for the reddest objects in the photometric sample (i.e., $g-r > 3$), there seems to be very few galaxies with spectroscopic information. We notice that galaxies with such extreme colours may not be well represented by the results presented through this section.

Top right panel of Figure 2 shows the normalized magnitude distribution for the samples introduced before. The photometric depth of the S-PLUS survey (a.k.a., “S-PLUS/photometry”) is represented by the red histogram, whereas that of the spectroscopic sample (a.k.a., “S-PLUS/spectra”) is represented by the blue histogram. In order to be self-consistent when comparing magnitudes among datasets (i.e., due to differences in filters and photometric apertures), we have decided to use the S-PLUS magnitudes to define the photometric-depth of both samples. Therefore, the blue histogram represents the S-PLUS magnitudes for those galaxies detected in the S-PLUS survey with a spectroscopic redshift measurement. It is worth mentioning that this comparison serves to understand whether the spectroscopic sample utilized in this work (i.e., to characterize the expected photo-z precision) can be considered representative of the entire S-PLUS survey. As expected, whereas the photometric sample (i.e., red histogram) shows a smooth and single-peak distribution at a around $r = 20.5-21.0$ magnitudes, the spectroscopic sample is multi-modal and shallower, with a main peak at a magnitude $r \sim 19.5$ and a secondary (less pronounced) peak at a magnitude $r \sim 20.5$. This comparison can be interpreted as follows: Although it is true

the majority of galaxies in the spectroscopic sample is clustered in brighter magnitude bins (i.e., $18 < r < 20$), this may still have a large number of galaxies with magnitudes close to the S-PLUS limiting magnitude (i.e., rightmost tail reaching magnitude $r = 22$). In other words, the spectroscopic sample shows a high density of galaxies at those intermediate magnitudes where the S-PLUS survey can still detect galaxies with a high signal-to-noise and, a progressively decreasing sample of galaxies with spectroscopic information in the close to the survey detection limit where the quality and completeness of our photometry could be compromised. Finally, it is worth mentioning that this heterogeneity in the data does not represent an issue for the scope of this paper⁴, but might affect other redshift estimates based on learning process where resembling samples are needed for training purposes at all magnitude and redshift bins.

The bottom left panel of Figure 2 shows the redshift distribution for both samples. As before, the blue histogram (a.k.a., “S-PLUS/spectra”) corresponds to the subsample of galaxies in the spectroscopic redshift sample detected by the S-PLUS observations whereas the red histogram (a.k.a., “spectroscopy”) to the whole spectroscopic sample within the S-PLUS footprint. This comparison serves to understand the selection effect in redshift space (i.e., the completeness) imposed by the photometric depth of the S-PLUS observations. As clearly seen in this panel, while most galaxies at $z < 0.5$ are detected in the S-PLUS images, there is a large fraction of galaxies missing at $z > 0.5$. This is a clear sign of a selection function in redshift for the S-PLUS data. While this issue will be fully address in Section 6.3, here we can conclude the following. The spectroscopic sample utilized in this work seems to be sufficient for the scope of this paper because, unlike most surveys, here it is the observations that limit the depth of the spectroscopic sample and not the other way around. In other words, we might be able to characterize the photo- z precision for those $z > 0.5$ galaxies typically detected in S-PLUS to the photometric depth of its observations.

Finally, the bottom right panel of Figure 2 shows the spectral-type distribution of galaxies as a function of redshift. As before, these samples correspond solely to the galaxies in the spectroscopic sample detected in the S-PLUS observations. In order to facilitate its visualization, the red histogram corresponds to those galaxies classified by the BPZ2 code as early/quiescent types and the blue histograms to those classified as late/star-forming types. In order to be able to know the spectral-type of each galaxy in the spectroscopic sample, we did a similar exercise as that presented at the beginning of this section. We ran the BPZ2 code using the ONLY_TYPE = YES mode, to redshift all galaxy models in its library to the corresponding spectroscopic redshift value. Based on the S-PLUS photometry for each galaxy, the BPZ2 code estimated the most likely model. We finally labeled as “early” to those galaxies with a spectral-type $T_b \leq 6.5$ and as “late” to those with a spectral-type $T_b > 6.5$. The results from this figure can be interpreted as follows: As expected, early-type galaxies are more smoothly distributed over the entire redshift range, presenting two prominent peaks at $z = 0.15$

& $z = 0.55$; being the last one associated with the Luminous Red Galaxies (i.e., LRG). Beyond that, the S-PLUS selection function makes the distribution to decline rapidly, with a very limited sample beyond $z = 1.0$. On the other hand, we observe that intermediate- and late-type galaxies are more clustered at $z < 0.25$, with a steadily shrinking sample at $z \geq 0.25$. Although it is true that at $z \geq 0.5$ the spectroscopic sample utilized in this work will be dominated by red/early-type galaxies, the number of blue/late-type galaxies will still be large enough to guarantee a robust characterization of our photo- z at those redshift ranges. We refer the reader to Sec. 6.3 for a further discussion on this topic.

In the light of what has been presented and discussed above, we consider that the spectroscopic sample utilized in this paper can be considered as representative (i.e., colour, magnitude, redshift and spectral-type terms) for the universe observed by the S-PLUS survey. Therefore, the characterization of the photo- z performance we present in the following sections, can be considered as a good estimate of the survey.

3 PHOTOMETRIC REDSHIFTS

A photometric redshift (hereafter photo- z) represents an indirect estimate of the distance to an extragalactic source based on a discrete assemble of fluxes (or magnitudes) measured for an astronomical object when it is observed through a particular filter system. Along with the distance (or redshift), this technique typically also provides an estimate of the spectral energy distribution (i.e., SED) of the source in consideration. The combination of these two pieces of information (e.g., redshift and SED) makes this technique ideal for galaxy evolution studies. From its first application in the 1960s (Baum 1962), this technique has experienced a relatively long history. Nowadays, photo- z have become an essential tool in modern astronomy since they represent a quick and almost inexpensive way of retrieving redshift estimates and SED identification for a large amount of extragalactic sources in a relatively small amount of observational time.

Although it is true that redshift estimations from galaxy colours are more uncertain than those obtained directly from a spectrum, this situation has been gradually improved. Multi medium- or narrow-band surveys such as COMBO-17 (Wolf et al. 2001), COSMOS-21 (Taniguchi et al. 2007), ALHAMBRA (Moles et al. 2008), COSMOS-30 (Ilbert et al. 2009), S-PLUS (Mendes de Oliveria et al., (subm.)) or J-PLUS (Cenarro et al. 2019), can now achieve statistical photo- z uncertainties of $\Delta z / (1+z) = 0.01$ for high S/N galaxies. The new generation of multi-band surveys, such as J-PAS (Benítez et al. 2014) and PAU (Martí et al. 2014b), which utilizes a photometric systems composed by ~ 60 100Å-width narrow-band filters, can provide “very low resolution spectra” achieving statistical photo- z uncertainties as low as $\Delta z / (1+z) = 0.003$ for millions of galaxies, down to a magnitude $r \sim 22.5$ (Ascaso et al. 2016, Eriksen et al. 2018).

As discussed in Zheng & Zhang (2012) and in Carrasco Kind & Brunner (2014b), current photo- z techniques can be broadly divided in two main categories: SED-fitting and training-based algorithms. On the one side, template fitting

⁴ We are adopting an SED-fitting approach to compute photo- z .

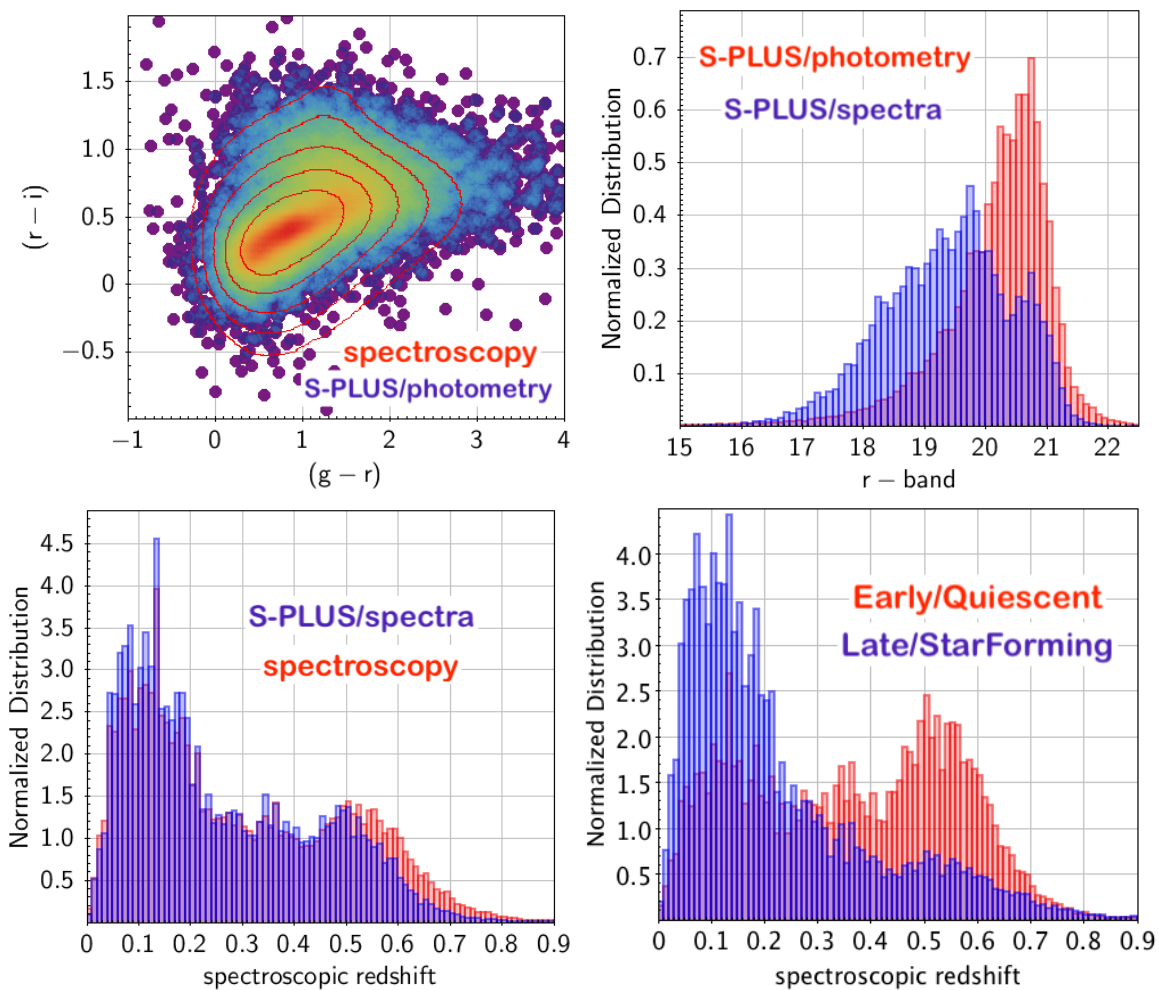


Figure 2. Validation of the spectroscopic redshift sample. Top-left: comparison of the colour-colour distribution for both the spectroscopic redshift (contours) and the photometric (dots) samples. Top-right: Magnitude distribution of galaxies in the spectroscopic (blue) and photometric (red) samples. Bottom-left: Redshift distribution of both samples. Red histogram corresponds to all galaxies with spectroscopic redshift information within the S-PLUS footprint. Blue histogram represents the fraction of those galaxies detected in the S-PLUS observations. Bottom-right: Spectral-type distribution of galaxies as a function of redshift, with early/quiescent galaxies in red and late/starforming galaxies in blue.

approaches such as BPZ (Benítez 2000), EAZY (Brammer et al. 2008), GAZELLE (Kotulla et al. 2009), GOODZ (Dahlen et al. 2010), Hyperz (Bolzonella et al. 2000), Le Phare (Arnouts et al. 2002; Ilbert et al. 2006), LRT (Assef et al. 2008, Assef et al. 2010), ZEBRA (Feldmann et al. 2006), IMPZ (Babbedge et al. 2004) and CZR (Richards et al. 2001; Weinstein et al. 2004), estimate photo-z by finding the best match between the observed and the predicted magnitudes (or colours) of galaxies according to a library of galaxy models (or SED templates). The main advantage of these template-based codes is that they can be applied without needing large and high-quality spectroscopic training samples. However, inaccurate estimations of the filter transmission curves or faulty libraries of templates may severely affect the performance of these techniques.

On the other side, machine learning methods such as PR (Connolly et al. 1995; Hsieh et al. 2005), NN/kNN (Ball et al. 2008), KR (Wang et al. 2007; Wolf 2009), ArborZ (Gerdes et al. 2010), GPs (Way et al. 2009; Bonfield et al. 2010), MS (Budavári 2009), ANNs (Firth et al. 2003; Collister & Lahav

2004), MLP (Vanzella et al. 2004), SVMs (Wadadekar 2005), WGE (Laurino et al. 2011), SCA (Freeman et al. 2009), TPZ (Carrasco Kind & Brunner 2013), SOMz (Carrasco Kind & Brunner 2014a), among others, have the advantage of being easier to include extra information (apart from magnitudes and colours), such as galaxy profiles or concentrations in the computation of redshifts. However, these methodologies are only reliable within the limits of the training dataset, making uncertain its extrapolation to different magnitude, redshift or wavelength ranges. Therefore, they are highly disadvised for surveys or datasets with small training samples.

As emphasized before, this paper aims at describing the usability of the S-PLUS photometric redshifts in extragalactic studies. Therefore, rather than formatting this work as another photo-z-challenge paper (where the performance of several codes are presented), we have preferred to apply solely a single well-tested and well-known photometric redshift code, keeping the focus on the data themselves rather than on the specific systematics each codes may display. A

discussion about the benefits of combining several photo- z codes for the S-PLUS data and the optimal way of combining such information will be addressed in a separate paper.

Through the following sections, we provide a description of the potential of the S-PLUS multi-band photometric data for SED and redshift estimates of galaxies in the nearby Universe and we discuss the role it can play in extragalactic astronomy. We start by describing in 3.1 and 3.2 the code we have used to compute photometric redshifts and several updates necessary to adequate the software to the needs of S-PLUS. In 3.3 we described the metric adopted to characterize the performance of our estimates. Section 3.4 presents a throughout description of the results achieved as a function of a number of variables, such as magnitude, redshift, spectral-type and Odds. Section 3.5 we calculate the photo- z depth of S-PLUS, providing a forecast of the number of expected galaxies in the survey with a given photo- z precision. Section 3.6 is devoted to compare our results with those from other previous works on the Stripe-82 using similar datasets. In Section 3.7, we quantify the improvement in our estimates due to the increase in the wavelength resolution provided by the 7 narrow-band filters. Finally, Section 3.8 highlights the possibility of using specific redshift windows where the photo- z precision gets improved due to the detection of emission-lines from galaxies.

3.1 The BPZ2 code.

We rely on the Bayesian Photometric Redshift (BPZ2) code (Benítez (2000), Coe et al. (2006)) to compute our photo- z estimates. BPZ2 is a Bayesian template-fitting code where a likelihood function coming from the comparison between data (D) and models (T) is weighted by an empirical luminosity-based prior, as indicated in Eq. 1:

$$p(z|D, m_0) \propto p(z, T|m_0) \times p(D|z, T) \quad (1)$$

where $p(z|D, m_0)$ represents the full posterior distribution (or PDF), $p(z, T|m_0)$ the likelihood, $p(D|z, T)$ the prior and m_0 the apparent magnitude of the galaxy. As discussed below, these PDFs surpass traditional point-like estimates, enhancing the reliability of statistical analysis based on photo- z . The characterization of these distribution functions will be addressed in Section 3.3 and Section 4.

In this work, we use the (BPZ2) code which has already been applied to other astronomical surveys (e.g., ALHAMBRA (Molino et al. 2014), J-PAS (Ascaso et al. 2016), CLASH (Molino et al. 2017) and J-PLUS (Molino et al. 2019)) showing excellent results. Compared to its public version⁵, BPZ2 includes the following updates: it is computationally faster and its photo- z estimates are more robust. It includes a new library of galaxy templates composed by 5 early- and 9 late-type models (see Section 3.2), including emission lines and dust extinction. The opacity of the intergalactic medium is applied as described in Madau (1995). In addition, it provides an estimate of both the absolute magnitude and the stellar mass content of galaxies based on

the most likely redshift and spectral-type solution. PDFs are now stored using a Hierarchical Data Format (HDF5), which is more efficient than the previous ASCII files. It also includes new priors derived from several datasets and initially applied to the ALHAMBRA survey. We refer the reader to Molino et al. (2014) for more details about BPZ2.

As discussed by several authors (e.g., Benítez et al. (2009a), Bordoloi et al. (2010), Martí et al. (2014a), The LSST Dark Energy Science Collaboration et al. (2018), among others), high-precision cosmological studies based on photometric redshifts require these estimates to be robust; as much in terms of precision (i.e., small σ_z) as in terms of accuracy (i.e., $\mu_z \sim 0$), and a limited fraction of catastrophic outliers. As demonstrated in several works, the Odds parameter from the BPZ code serves precisely to that purpose (Benítez et al. (2009a), Molino et al. (2014), Jiménez-Teja et al. (2015), Ascaso et al. (2015)). As defined in Benítez (2000), the Odds of a galaxy corresponds to the ratio between the integrated probability within a redshift interval (i.e., Δ_z) around the most probable value (i.e., z_p) in the probability distribution function (i.e., $p(z)$), over the entire probability distribution. This expression is presented as follows:

$$Odds = \frac{\int_{z_p - \Delta_z}^{z_p + \Delta_z} p(z) dz}{\int_{z_1}^{z_2} p(z) dz}, \quad (2)$$

where z_1 and z_2 correspond to the minimum and maximum redshift values, respectively, considered in the analysis. Based on equation 2, narrow distributions will result in values close to 1 since much of their integrated probabilities will be contained in the redshift interval Δ_z . Oppositely, very broad or multi-modal distributions will result in values close to 0 since the fraction of their integrated probability will be small. Therefore, the Odds can be understood as a quality parameter where, the closer to 1, the more reliable (i.e, the less uncertain) the photo- z determination is.

Finally, BPZ2 allows the user to fine-tune the redshift interval over which to integrate the Odds, calibrating these estimates to the characteristic of any dataset. The integration interval has typically been defined as twice the expected precision of the photo- z estimates: $\Delta_z = 2 \times \sigma_z$. In its previous version, BPZ2 used a fixed $\Delta_z = 0.06$ interval, since that was the typical precision of photo- z estimates at the time (Sawicki et al. (1997), Fernández-Soto et al. (1999), Csabai et al. (2003), Coe et al. (2006), among others). With the tremendous improvement in the precision of these photo- z estimates from surveys including many medium and/or narrow-passbands, the definition of this integration interval had to be updated. In this work, we adopted an interval $\Delta_z = 0.02$, since this is the averaged expected precision for most galaxies in the nearby Universe (see Section 3.4).

3.2 Updates for the nearby Universe.

The BPZ2 code has been applied to a large number of datasets, from intermediate (Jouvel et al. (2014), Nieves-Seoane et al. (2017)) to high redshift (Zheng et al. (2012), Zitrin et al. (2014), Jiménez-Teja et al. (2015)). Although

⁵ <http://www.stsci.edu/~dcoeb/BPZ/>

BPZ2 has always excelled as one of the most robust photo- z codes (e.g., Hildebrandt et al. (2010)), it has been reported by several authors (internal communications) that it underperforms in the nearby Universe. Whereas it performs well in terms of precision (i.e., small σ_z), it may underperform in terms of accuracy (i.e., $\mu_z \neq 0$). In other words, BPZ2 may successfully identify galaxies at the same redshift (e.g., in a cluster) but assigning to them a biased redshift. As concluded in Molino et al. (2017), from a systematic study of galaxies in massive clusters using BPZ2, this effect can be explained as a consequence of an incomplete library of SED models. In the absence of proper models, BPZ2 may compensate the differences in colour between models and observations by redshifting or blueshifting the templates, until reaching a mathematical minimization.

While characterizing the performance of our photometric redshifts, we noticed a similar effect. After binning the galaxies in magnitude and/or in redshift, we discovered that most early-type galaxies retrieved a rather large bias in the error distribution. A deeper inspection showed that the redshift-colour space for early-type galaxies was not properly covered by the previous templates. In the light of this event, we decided to incorporate additional models in our library and test its new performance. Fortunately, we noticed these models increased the accuracy of our estimates, completely eliminating the previous bias (i.e., $\mu_z < 0.1\%$) at all magnitude and redshift ranges.

Additionally, we realized that the precision (i.e., σ_z) obtained for the early-type models was poorer than that obtained for the late-type ones. Due to the depth of our images, we noticed the signal was limited (if any) at the bluest wavelengths for the most red galaxies in our fields. Effect that could limit the performance of our photo- z estimates due to the fact that we may be relying on a subset of filters for its computation. In order to disentangle the effect of a limited signal from the representativeness of these models among red galaxies, we make use of the ALHAMBRA-Gold catalog⁶. This catalog includes a sample of ~ 1000 early-type galaxies observed with a 23-band optical filter system to a depth of $r \sim 25$ magnitudes. By selecting galaxies down to a magnitude similar to that of the S-PLUS (i.e., $r < 22$), we assure all galaxies in ALHAMBRA have a high signal-to-noise photometry in all the red and blue filters. Based on the ALHAMBRA photometry (Molino et al. 2014), we ran BPZ2 using this new library of SED models. This new library improved the previous precision, presented in Molino et al. (2014), by a factor of 2.5 for galaxies with a magnitude $r < 17$, and a factor of 1.5 for galaxies with magnitudes in between $17 < r < 21$. Additionally, it reduced, up to an order of magnitude, the bias for galaxies at low-redshift ($\mu_z \sim 0.00$ for $z < 0.3$). These results served to prove that the limited performance of our new red templates was solely due to limited photometric-depth of the S-PLUS observations. The new library of SED models, utilized in this work, is shown in Figure 3.

Finally, the previous BPZ2 prior was extended to include galaxies with magnitudes brighter than $r < 18$. So, adequat-

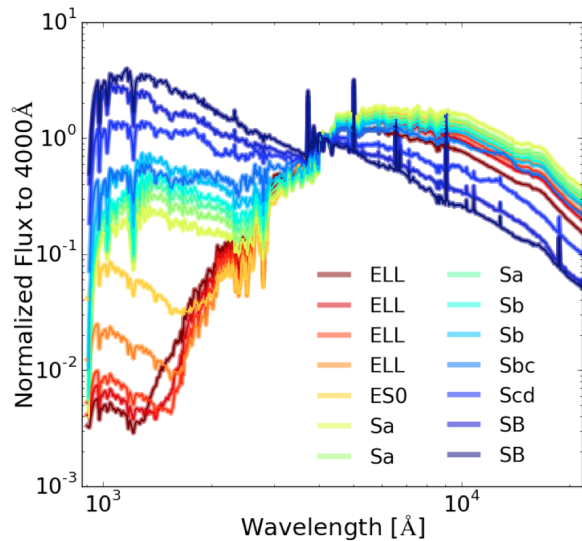


Figure 3. Library of SED models utilized in this work. In order to improve the colour coverage of low-to-intermediate redshift early-type galaxies, 4 additional templates were incorporated to the previous library of BPZ2. Models include emission lines and dust extinction.

ing it to the needs of the new local universe multi-band photometric redshift surveys such as S-PLUS and J-PLUS.

3.3 Evaluation Metric.

Although there are several recent works where elaborated metrics are defined for the characterization of photometric redshift estimates (e.g., Carrasco Kind & Brunner (2014b) and Sánchez et al. (2014)), in this work we prefer to adopt a simpler, more intuitive metric as that presented in Molino et al. (2014). We address the characterization of our photometric redshifts in two independent steps. Whereas in Section 3.4 we treat them as single-point estimates (i.e., based on the most likely redshift solution), in Section 4 we analyze its performance treating them as probability distribution functions (PDFs).

For the description of photometric redshift as single-point estimates, we rely on the Normalized Median Absolute Deviation (NMAD; see Eq. 3), which represents a robust measurement of the accuracy reached by a set of estimates (Brammer et al. 2008). It is worth stressing that a typical photometric redshift error distribution has extended tails, clearly departing from a pure Gaussian distribution, in addition to a relatively large fraction of outliers. The NMAD estimator manages to get a stable estimate of the spread of the core of the photo- z distribution without being affected by catastrophic errors. The accuracy of this estimator (i.e., σ_{NMAD}) is defined as:

$$\sigma_{NMAD} = 1.48 \times \text{median}\left(\frac{|\delta z - \text{median}(\delta z)|}{1 + z_s}\right) \quad (3)$$

being $\delta z = z_b - z_s$, z_b the Bayesian photometric redshift

⁶ <http://cosmo.iaa.es/content/ALHAMBRA-Gold-catalog>

and z_s the spectroscopic redshift.⁷ Along with this, it is also important to quantify its precision (μ) to identify any systematic bias in the redshift estimations. Finally, we describe the expected fraction of catastrophic errors (η) which, in this work, is defined as:

$$\eta = \frac{|\delta z|}{1 + z_s} > 5 \times \sigma_{NMAD} \quad (4)$$

Finally, for the description of our photometric redshifts as probability distribution functions, we make use, in Section 4.1, of the Highest Probability Density (HPD) to measure the reliability of our PDFs encoding real redshift uncertainties.

3.4 Photo-z Performance.

Through the following subsections, we present a number of tests describing the performance of the S-PLUS photometric redshifts based on the observations described in Section 2. These analyses describe the observed performance as a function of the r -band magnitude, the redshift and the **Odds** parameter from the BPZ2 code. In all three cases, we will first estimate the average precision for all types of galaxies, and then splitting the sample in different spectral-types (i.e., early/red and late/blue types)⁸. Later on, in subsection 3.4.3, we will further elaborate these analyses showing the expected performance of our photo-z in a multi-dimensional space, through the combination of all the aforementioned variables. These diagrams will serve to identify sub-regions where the photo-z performance gets improved due to the given wavelength-resolution of the filter system (see Section 3.8 for a further discussion). Finally, in Section 3.5, and based on the **Odds** parameter, we will forecast the photometric-redshift-depth of the survey, i.e., predicting the total amount of galaxies expected in the S-PLUS survey with a minimum (maximum) photometric redshift precision as a function of the magnitude and/or redshift.

3.4.1 As a function of the magnitude and redshift.

We study the dependence of the photo-z precision as a function of the apparent r -band magnitude and redshift. Firstly, this analysis serves to understand how our photo-z estimates become affected by the photometric noise in our data. Secondly, it also reflects the importance of the (inhomogeneous) wavelength resolution of our filter system sampling the SED of sources, since we expect to detect galaxies with similar apparent magnitudes but with different redshifts. For this exercise we define several magnitude bins ranging from $14.5 < r < 21.5$, and redshift values in between $0 < z < 1$. These limits are chosen with the purpose of avoiding both very bright and too faint galaxies whose photometry could be compromised.

Although a full description of the results extracted from

this exercise can be found in Table A1, Table A2 & Table A3, here we extract a few interesting results. Averaging over all types of galaxies and redshifts, we find a precision of $\sigma_z \sim 1\%$, $\sigma_z \sim 2\%$ and $\sigma_z \sim 3\%$ for galaxies with apparent magnitudes $r < 17$, $r < 19$ and $r < 21$, respectively. This behaviour is expected since it reflects that the lower the signal-to-noise of the detection is, the more uncertain becomes its redshift estimation. In addition, it is observed a negligible bias ($\mu_z \sim 0.1\%$) as a function of the magnitude, which indicates that the photo-z estimates are very accurate (see discussion in Section 3.1). Interestingly, for the brightest magnitude bins ($r < 16$), we find that early-type galaxies reach a superb precision of $\sigma_z \sim 0.6\%$; reinforcing the role of S-PLUS for clustering detecting in the nearby Universe. In Figure 4 we show the performance of our photo-z estimates for three different magnitude intervals ($r < 17$, $r < 19$ and $r < 21$). Similarly, we find a precision of $\sigma_z \sim 1.5\%$ and $\sigma_z \sim 3\%$ for galaxies with a redshift $z < 0.05$ & $z < 0.5$, respectively. Interestingly, we observe that early-type galaxies with redshifts below $z < 0.1$ or $z < 0.5$ reach a precision of $\sigma_z \sim 1.0\%$ or $\sigma_z \sim 2.0\%$, respectively. Finally, it is worth mentioning that the obtained fraction of catastrophic outliers (defined as Eq.4) was always smaller than a few percents, with a clear dependence with the magnitude and the redshift.

3.4.2 As a function of the Odds.

As discussed in Section 3.1, the **Odds** parameter renders possible the selection of clean samples of galaxies with precise (small σ_z) and accurate (small μ_z) photo-z estimates. We analyze the performance of our photo-z estimates as a function of this parameter, as much globally as for different spectral-types. In Figure 5, we present the resulting photo-z error distribution function for samples with different **Odds** cuts. As indicated in the legend, the higher the **Odds** value is, the narrower the distribution is or, in other words, the more accurate the photo-z predictions are. A precision of $\sigma_z = 0.8\%$, 1.5% and 2.5% is found for galaxies with **Odds** > 0.9, **Odds** > 0.6 and **Odds** > 0.2, respectively. As in the previous section, we find a very small fraction of catastrophic outliers always smaller than a few percents. Additionally, Tables A1 & A4 describe in detail the observed performance as a function of the **Odds**.

3.4.3 As a function of the magnitude, redshift and Odds.

Finally, in this section we analyze the performance of our photo-z estimates combining different variables: r -band magnitudes, redshift and the **Odds** parameter. To motivate this exercise, it is worth mentioning that, by selecting specific bins in the magnitude-redshift space, it turns out possible to better understand the limitation in the photo-z estimates given by the photometric-depth or the filter-system of a survey. For example, it is expected that within a given magnitude bin there will exist galaxies at different redshifts. By selecting galaxies with a specific magnitude (i.e., signal-to-noise), it is feasible to isolate the contribution to the photometric redshift uncertainties coming from the wavelength resolution given by our filter system. Similarly, by selecting galaxies at the same redshift interval, we can isolate the im-

⁷ For the sake of keeping the notation simple, we will adopt through this paper σ or σ_z when referring to the σ_{NMAD}

⁸ The spectral-type classification is done according to the most likely template selected by the BPZ2 code using the `ONLY_TYPE=yes` mode

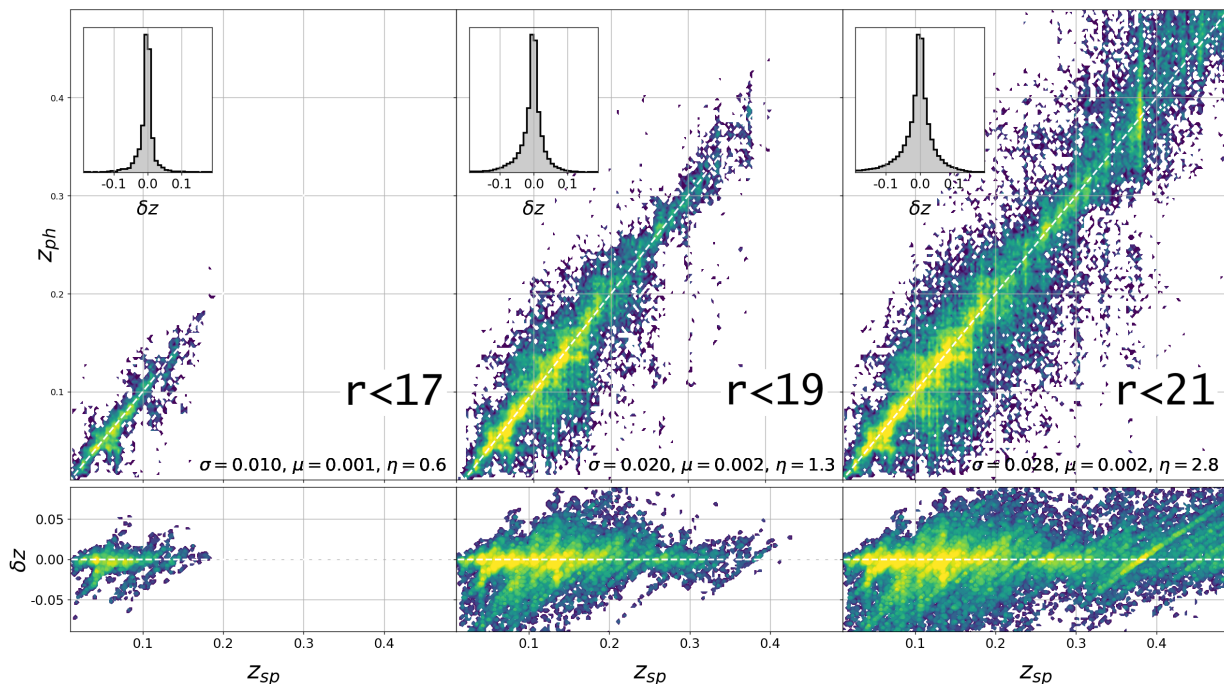


Figure 4. Photometric Redshift Precision of the S-PLUS survey as a function of the r -band magnitude, for three different intervals. Colours correspond to a logarithmic number density of sources. As indicated in the inner labels, the expected dispersion for galaxies with magnitudes brighter than $r < 17$, $r < 19$ & $r < 21$ is $\delta z/(1+z) < 0.01$, $\delta z/(1+z) < 0.02$ & $\delta z/(1+z) < 0.03$, respectively. Top left inner panel shows the error distribution. The symmetry of these distributions indicate that the total accumulated bias is always $< 1\%$.

part of the sources detected with different signal-to-noise in the photo- z estimates.

In Figure 6 we represent the observed photo- z precision as a function of the r -band magnitude, redshift and the Odds parameter. From left to right, a selection criteria of $\text{Odds} > 0.0$, $\text{Odds} > 0.5$ and $\text{Odds} > 0.9$ has been imposed. The photo- z precision is colour-coded as indicated by the vertical colour-bar. As expected, on the one hand, an overall improvement at all magnitude and redshift bins is observed as galaxies with a higher Odds value are selected. Therefore, it becomes feasible to retrieve samples of galaxies with a given maximum photo- z error at specific magnitude-redshift windows. On the other hand, in every individual subsample, the average precision decreases as we move upwards or rightwards, since galaxies in those bins will be progressively fainter. Interestingly, however, there are bins in which the precision abruptly improves (or worsen). These fluctuations reflect the inhomogeneous detectability of spectral features by our filter system. An example of these windows is presented in Section 3.8. These diagrams make possible to understand which the expected precision for the S-PLUS photo- z estimates is within specific magnitude-redshift bins.

3.4.4 Spectral-type misclassification.

In this section we investigate how the uncertainties in the redshift estimations may affect the spectral-type classification of sources or, in other words, how uncertainties in the redshift space may translate into uncertainties in the spectral-type space. This is an important piece of informa-

tion when deriving spectral-type-dependent statistical analysis, since it represents the capacity of distinguishing among models, acting like a spectral-type resolution indicator.

In order to cope with this goal, we used once more the spectroscopic sample presented in Section 2.3.2, running the BPZ2 code twice on it. First, using the ONLY_TYPE = YES mode redshifting all SED models to the exact redshift value. Then, we use its normal mode allowing BPZ2 to predict the most likely redshift for each galaxy according to the S-PLUS data. Since all other configuration parameters but this are kept the same during both runs, the so-observed variations in the spectral-type classification come from the uncertainties in redshift space. Trying to make this analysis more useful, we present the results as a function of the r -band magnitude (r), the spectroscopic redshift (z) and the Odds parameter (O). Likewise, we split each one of these groups in three subsamples ($r < 17, 19, 21$, $z < 0.2, 0.4, 0.6$ and $O > 0.0, 0.5, 0.9$), to see how the precision classifying the spectral-type of sources evolves with these variables. Finally, in order to facilitate the visualization of these results, as illustrated in Figure 7, we rely on simple confusion matrices where the initial (using spectroscopic redshifts) and final (using photometric redshifts) classifications are displayed, respectively, horizontal and vertically. The normalized number density of sources is colour-coded in each panel.

We observe that galaxies with bright magnitudes (top left), at low redshift (intermediate left) and with high Odds values (bottom right) preserve its original classification, since most of these galaxies fall in matrix diagonal. This is an expected result since that galaxy population typically

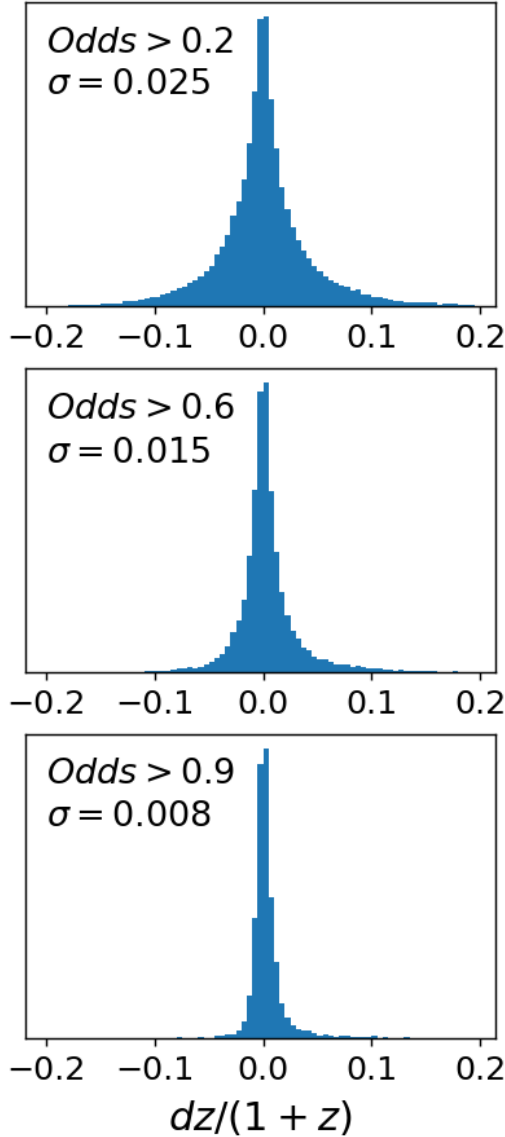


Figure 5. Photo- z error distribution function for samples with different **Odds** cuts. As indicated in the legend, the higher the **Odds** value, the narrower the distribution or, in other words, the more accurate the photo- z predictions. A precision of $\sigma_z=0.8\%$, 1.5% and 2.5% is found for galaxies with values **Odds** >0.9 , **Odds** >0.6 and **Odds** >0.2 , respectively.

has a high signal-to-noise photometry and many of the most important spectral-features (e.g., D4000) are still mapped by the filter system. These results progressively worsen as we move to fainter, higher in redshift and lower in **Odds** value galaxies. More galaxies populate non-diagonal positions in these confusion matrices, indicating the presence of misclassifications due to degeneracies. This is also expected as the photometric information available to constrain the redshift of galaxies becomes scarcer (i.e., early-type galaxies become to be non-detected in the bluest filters) or more uncertain (i.e., larger photometric noise), making more unfea-

sible to properly identify the real SED of source. In the worst case scenario presented here (i.e., galaxies with magnitude $r < 21$, $z < 0.6$ and **Odds** > 0.0), where the overall degeneracy among models is larger than in the previous cases, we highlight an interesting finding. Whereas early-type galaxies suffer a large degeneracy among them, late-type galaxy tend to preserve its original classification. This issue might be explained by the limited depth of the bluest filters, where faint red galaxies are typically non-detected due to the D4000-break while blue galaxies are still detected since their SEDs are more luminous at those wavelengths.

3.5 Photometric Redshift Depth.

In previous sections, the **Odds** parameter was used to retrieve galaxy samples with a common photometric redshift performance. Based on this piece of information, it turns out possible to characterize the so-called photometric redshift depth (hereafter, photo- z depth) of a survey; i.e., to forecast the number of galaxies expected in a survey with a certain photo- z precision, down to a certain magnitude. Although the analysis presented here is described solely in terms of the apparent r -band magnitude, the photometric redshift depth of a survey could be described in terms of other variables, such as redshift, morphology, spectral-type, or stellar-mass.

In order to estimate the photo- z depth of S-PLUS, we do the following exercise. Initially, we use the information presented in Section 3.4.2 and Table A1 to define four different **Odds** cuts (i.e., **Odds** >0.0 , **Odds** >0.4 , **Odds** >0.6 & **Odds** >0.8). This serves to split the photometric sample in groups of galaxies with a common photometric redshift precision: $\delta_z/(1+z) < 0.030$, $\delta_z/(1+z) < 0.020$, $\delta_z/(1+z) < 0.015$ & $\delta_z/(1+z) < 0.010$, respectively. Then, we count the number of galaxies per magnitude bin, before and after applying these **Odds** cuts. Thus, we estimate the fraction of galaxies within different magnitude bins, with a minimum **Odds** value. The results are illustrated on the left-hand side of Figure 8, where the completeness fraction of galaxies as a function of the r -band magnitude is shown. As seen from the inner panel, the photo- z precision is colour-coded as follows. From bottom to top, different lines correspond to galaxies with a photo- z precision $\delta_z/(1+z) < 0.008$, $\delta_z/(1+z) < 0.010$, < 0.015 , < 0.020 , < 0.025 and < 0.030 , respectively. From this figure we can draw the following conclusions: 80% of galaxies with a magnitude $r = 20.5$ are expected to have a photo- z error ≤ 0.025 , 50% with a photo- z error ≤ 0.020 at a magnitude $r = 19.5$ or 50% with a photo- z error ≤ 0.015 at a magnitude $r = 18.5$. Similarly, we find that 1 out of 10 galaxies at a magnitude $r = 18.5$ is expected to have a photo- z error ≤ 0.01 and that 5 out of 100 galaxies with magnitude $r = 18.0$ a photo- z error ≤ 0.008 .

In order to forecast the total expected number of galaxies in S-PLUS with a certain photometric redshift precision, after it completes the observation of the 8000 deg^2 , corresponding the MS region, it is necessary to estimate the expected number of galaxies in S-PLUS per magnitude bin and squared degree. To do so, we have selected all sources classified as galaxies from the 170 fields making the DR1 and computed its average number density as a function of the r -band magnitude; i.e., the averaged number of galaxies

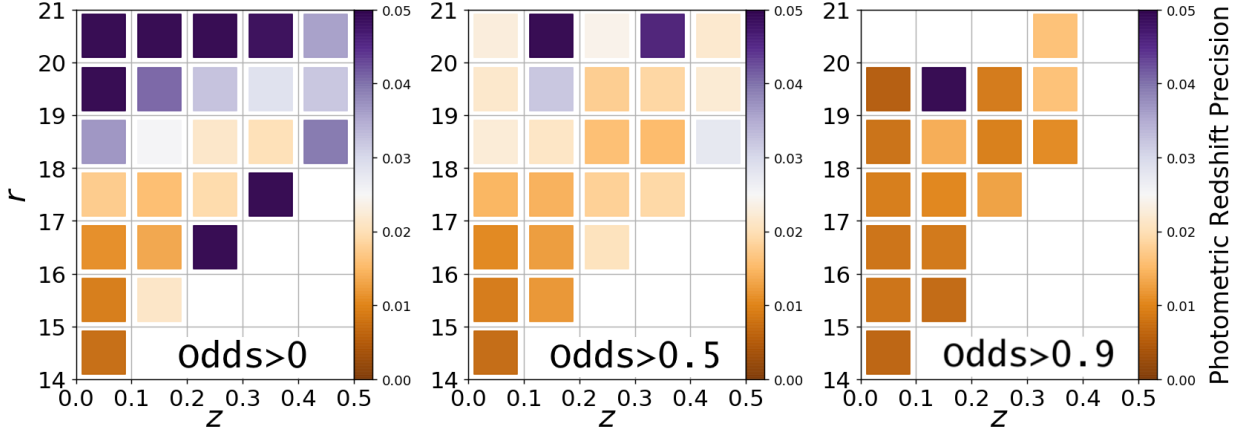


Figure 6. Photo-z precision for different Odds cuts

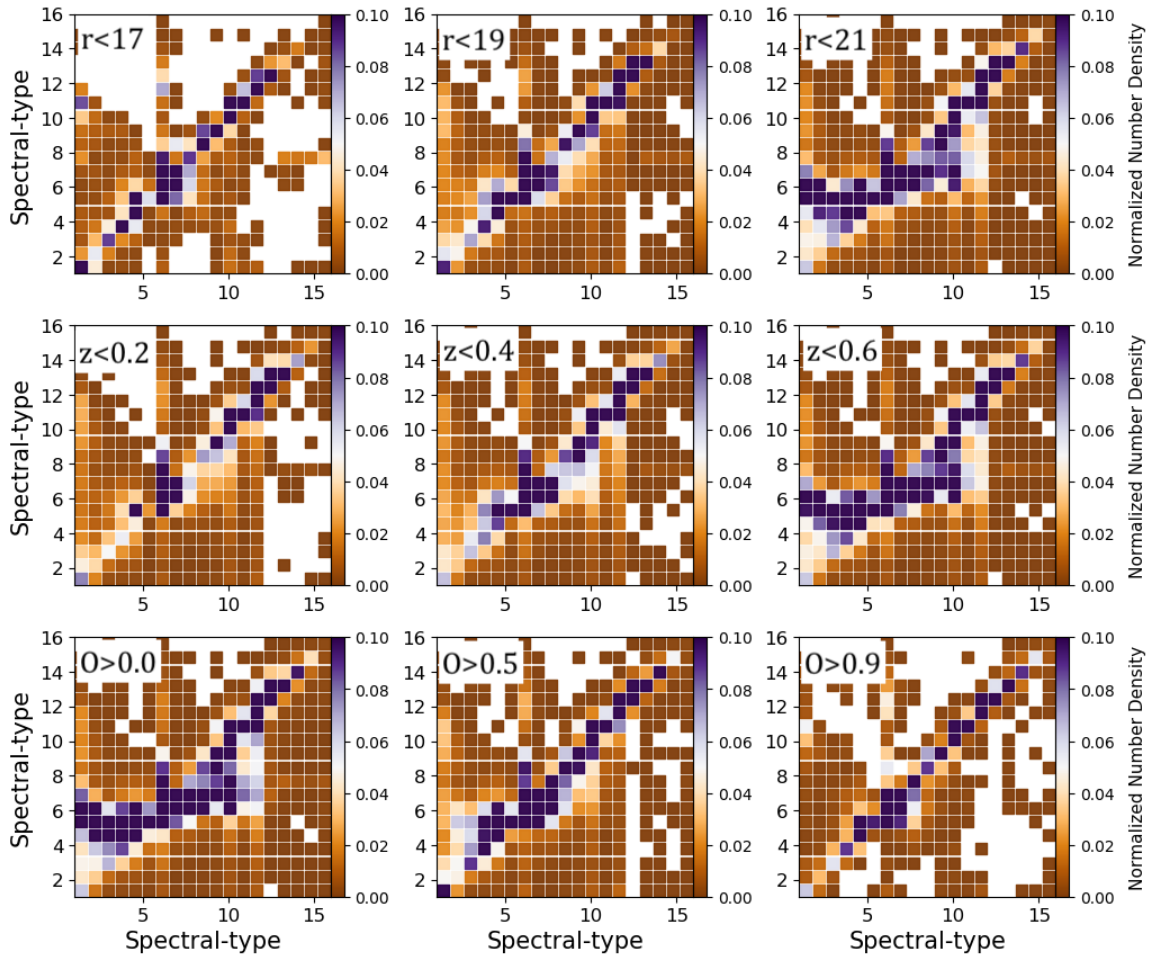


Figure 7. Spectral-type misclassification due to uncertainties in redshift space. Horizontal axes correspond to the classification based on spectroscopic redshifts and vertical axes to those based on photometric redshifts.

per degree squared. Finally, we have combined the previous completeness fraction with the so-estimated expected number of galaxies per magnitude bin in the 8000 deg^2 . The right panel from Figure 8 shows the expected cumulative distribution of galaxies between magnitudes $14 < r < 21$, where the photo- z precision is colour-coded adopting the previously used criteria. We find that, after S-PLUS completes its observations, a total of $\sim 1\text{M}$ of galaxies with a precision $\delta_z/(1+z) \leq 0.008$, $\sim 2\text{M}$ galaxies with a $\delta_z/(1+z) \leq 0.01$, 6.4M with a $\delta_z/(1+z) \leq 0.015$, 16M with a $\delta_z/(1+z) \leq 0.02$ and $\sim 32\text{M}$ galaxies with a $\delta_z/(1+z) \leq 0.025$.

Finally, these estimates correspond to the expected number of detectable galaxies in our survey which, in practice, does not need to correspond to the total number of galaxies in a given magnitude or redshift bin. As discussed in Section 6.3, in order to retrieve the real redshift distribution of galaxies in the Local Universe (i.e., $n(z)$), it is necessary first to compute the Completeness matrices as a function of the magnitude and redshift to, afterwards, correct the observed number counts to account for the non-detected galaxies in our images due to selection effects caused by the limited photometric depth of our observations⁹.

3.6 Comparison with other catalogs.

We take advantage that the Stripe-82 region has been observed by several other astronomical programs which have also performed multi-band photometry and derived photo- z estimates. To demonstrate the benefit of increasing the wavelength resolution (i.e., by including more filters) when estimating photo- z , a sample of $\sim 11\text{k}$ galaxies with magnitudes $r < 19.0$ was compiled to compare the performance of the photo- z . Stripe-82 Massive Galaxy Catalog (Bundy et al. 2015) combines SDSS/*ugriz* (complete down to a magnitude $r \sim 23.5\text{AB}$) and UKIDSS/*YJHKs* (complete down to a magnitude $r \sim 20\text{AB}$) data to derive photo- z in the Stripe-82¹⁰. Both datasets use the BPZ2 code for the redshift estimation. As seen in Figure 9, S-PLUS (in red) reaches a precision of $\delta_z/(1+z) < 0.016$ and a $\mu_z = 0.000$ for galaxies with a magnitude $r < 19.0$. For the exact same sample, Bundy et al. (2015) (in blue) reaches a precision of $\delta_z/(1+z) < 0.031$ and $\mu_z = 0.027$. Our results corresponds to an improvement of a factor of 2 in accuracy and a factor of 20 in the bias.

3.7 Importance of the 7 narrow-bands.

As demonstrated by many authors (e.g., see Figure B1 from Molino et al. (2014)), the reliability of photo- z determinations increases with the number of pass-bands which are used in the computation (see Hickson et al. (1994) or Benítez et al. (2009b) for an in-depth discussion). This is specially true in the case of medium-to-narrow pass-bands, since these allow a better sampling of the SED of sources. In this section, we want to quantify the benefit of including 7 additional narrow-bands (hereafter NBs) to classical $u, g, r,$

i, z broad-band (hereafter BBs) systems, when computing photo- z estimates as function of the apparent r -band magnitude and redshift.

To cope with this goal, we execute the BPZ2 code twice on the dataset presented in Section 2.2 & Section 2.4, adopting the following procedure. Initially, we run BPZ2 only with the 5 BB filters, forcing the code to ignore the photometry from the 7 NB filters. Subsequently, we rerun BPZ2 again but letting the code to use the entire dataset. Since the setting of BPZ2 is kept the same in both runs, the differences in the final performance simply reflect the importance of the wavelength-resolution when mapping out the SED of sources. The neat improvement in the redshift estimation given by the NBs is presented in Figure 10. In order to facilitate this comparison, we preferred to compute the ratio among precision σ_5/σ_{12} .

On the one hand, as shown in the left panel of Figure 10 where the precision is estimated separately for early- and late-type galaxies as a function of the r -band magnitude, including the additional 7 NBs leads to an improvement of a factor of 4 for galaxies with magnitudes $r < 15$, a factor of 2.5 for magnitudes $15 < r < 17$ and/or a factor of 1.7 for magnitudes $17 < r < 19$. This reflects the fact that when the signal-to-noise of the detections is high, photo- z estimates can dramatically improve those from classical systems. On the other hand, as shown in the right panel where the precision is estimated as a function of the redshift (z), a factor of 2 improvement is found for galaxies with $z < 0.1$ and a factor of 1.5 for $0.1 < z < 0.4$. Again, these results illustrate the enormous benefit of including additional narrow-bands to standard photometric systems. Interestingly, as pointed out in Molino et al. (2019), surveys such as SDSS, KiDS or DES based on standard broad-bands, cannot surpass a certain precision in their photo- z estimates irrespectively of the signal-to-noise of their observations. This limiting-factor comes from the limited wavelength resolution provided by the broad-bands, which causes a degeneracy in the colour-redshift space.

3.8 Redshift window opportunities.

As discussed in the Section 3.7, photometric redshift estimates computed from standard *ugriz* broad-band filter systems can be largely improved if they are complemented by medium-or-narrow pass-bands. Whereas broad-band filters mainly serve to constrain the continuum of the SED of sources, narrow-band filters allow the detection of other spectral-features (such as emission or absorption lines), which help to break (or to reduce) the colour-redshift degeneracies and, therefore, to downsize the photometric redshift uncertainties. As discussed in Benítez et al. (2014), the new generation of photometric redshift surveys (such as J-PAS (Benítez et al. 2014) and PAU (Martí et al. 2014b)), will utilize optimized filter systems made as a combination of broad and narrow pass-bands to get the best of each world and so maximize its performance at all magnitude and redshift ranges.

It is worth mentioning that the number and wavelength distribution of these narrow-band filters in a filter system will define a set of redshift windows within which a survey

⁹ Disconsidering other effects like the increase in bright stars at low galactic latitudes and/or regions with high galactic extinction.

¹⁰ <http://www.ucolick.org/~kbundy/massivegalaxies/s82-mgc-catalogs.html>

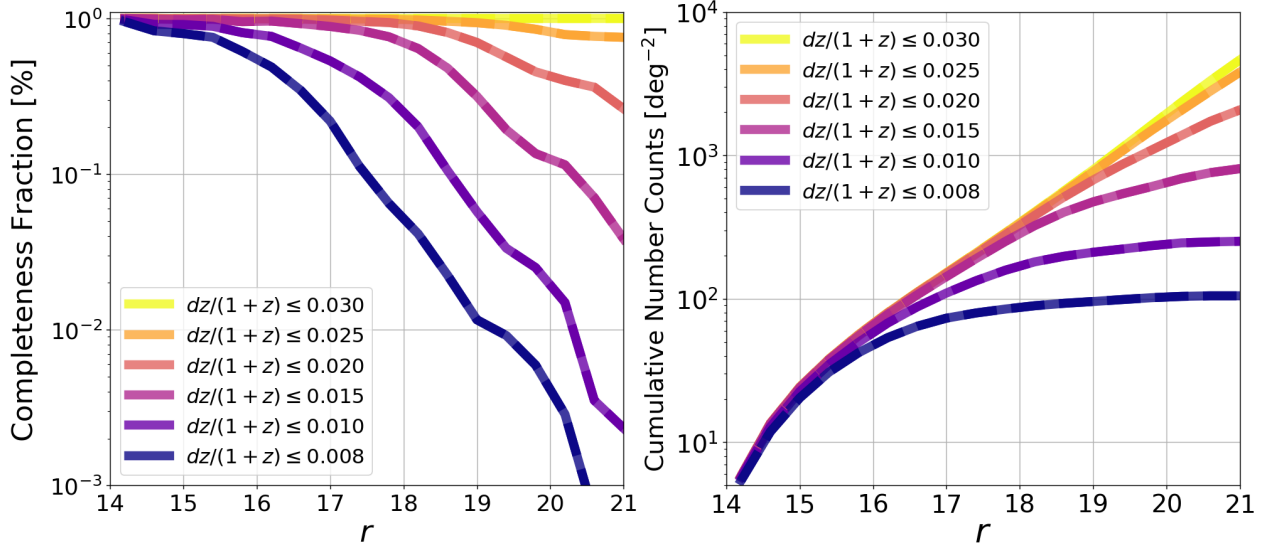


Figure 8. Photometric Redshift Depth. Left: Per one fraction of galaxies as a function of the r -band magnitude with a given photo- z precision. Right: Expected cumulative number of galaxies with a given photo- z precision and magnitude normalized to a 1 degree squared.

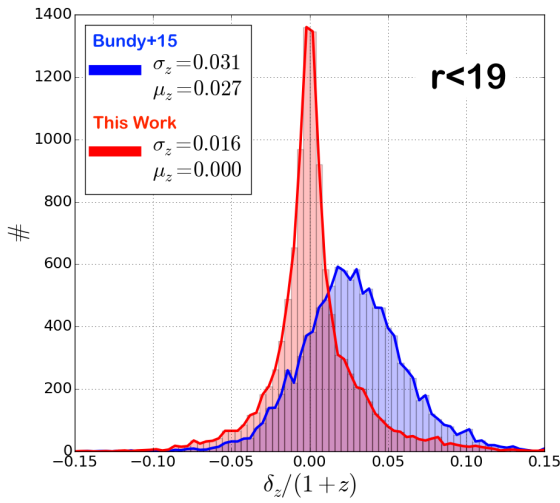


Figure 9. Photometric Redshift Performance compared to S82-MGC.

might be able to detect specific spectral features from astronomical sources¹¹. In this section, we cope with this goal, finding the redshift windows defined by the S-PLUS filter system, by relying on the `Odds` parameter since it encodes the performance of our estimates in a rather simple manner. As illustrated in the top panel of Figure 11, where the wavelength evolution of the emission-lines [OIII] and H α is shown as a function of redshift, there exist a redshift interval ($0.26 < z < 0.32$) where these emission-lines enter simultaneously both the $J0660$ and $J0861$ narrow-band filters, respectively.

This fact causes the photometric redshift estimates to

¹¹ If the signal-to-noise is large enough to allow the detection at that magnitude or redshift range.

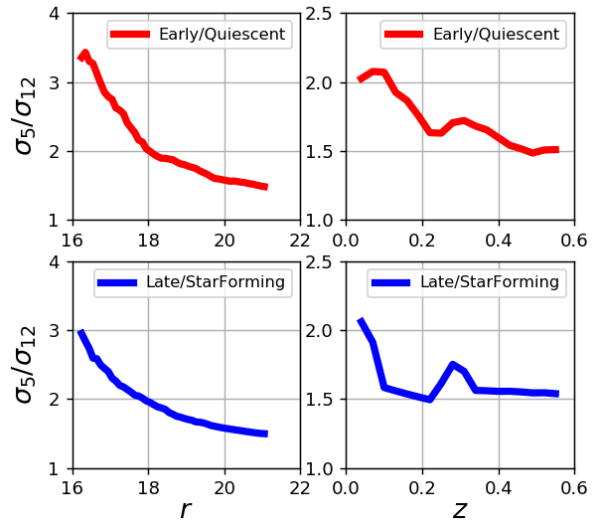


Figure 10. Performance ratio σ_5/σ_{12} when computing S-PLUS photo- z using 5 broad-band (σ_5) or 5 broad + 7 narrow-band (σ_{12}) filters. Ratio as a function of the r -band magnitude (left) and redshift (right), for quiescent/early-type (top) and star-forming/late-type galaxies (bottom) galaxies.

be more reliable and, therefore, to increase its `Odds` value. In the bottom panel of Figure 11, we represent the distribution of the obtained `Odds` values as a function of the redshift for all galaxies in our spectroscopic control sample. Colours represent the number density, being red densely and blue sparsely populated areas. As expected, the `Odds` distribution gets values close or equal to 1 for galaxies at $z < 0.15$ and declines steadily to lower values at $z > 0.15$. This behaviour is expected since most galaxies at low- z are detected with high signal-to-noise and high redshift galaxies tend to have a noisier photometry. Interestingly, in the exact redshift interval where the two emission-lines mentioned before

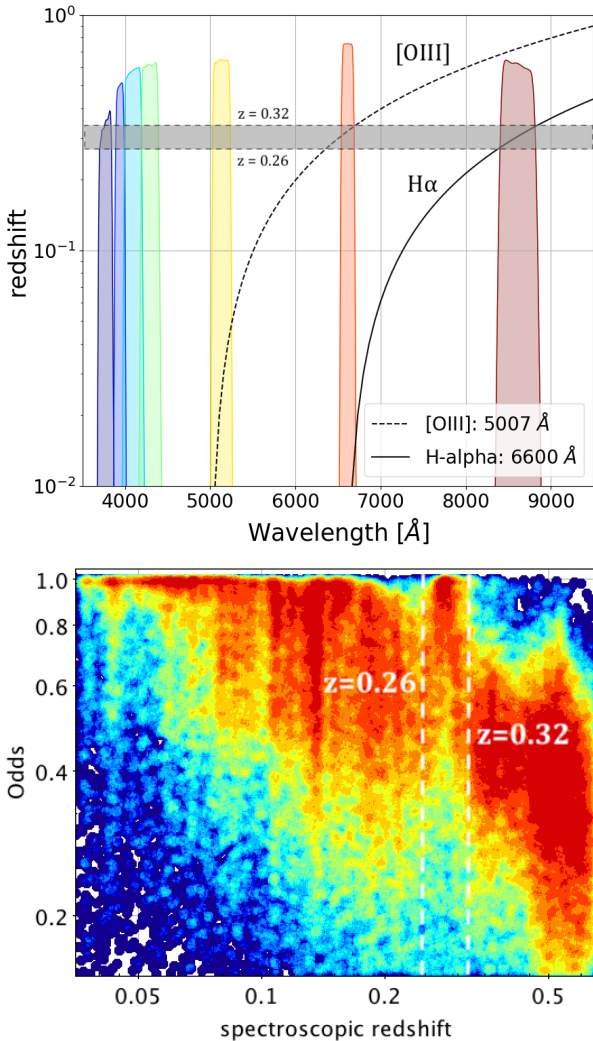


Figure 11. Redshift window opportunity. Top: The figure shows the simultaneous detection of the [OIII] and H α emission-lines, by the J0660 & J0861 narrow-band filters at a redshift interval $0.26 < z < 0.32$. Bottom: Distribution of the Odds values as a function of the redshift, for the $\sim 100k$ galaxies in the spectroscopic control sample. It is observed an upturn in the distribution at the aforementioned redshift interval. This very effect represents a boost in the photo-z estimates, bringing an opportunity to conduct statistical analysis.

are supposed to be simultaneously detected by the narrow-band filters ($0.26 < z < 0.32$), the Odds shows a clear upturn, passing from the expected Odds ~ 0.6 to Odds ~ 1.0 . This increase in the Odds value can be translated, according to the discussion stated in Section 3.4.2, into an improvement in the photo-z precision. Complementary to this discussion, as demonstrated in Figure 10 of Section 3.7, this effect is only observed when we include the 7 narrow-band filters in our filter system. This means that this redshift window is a distinctive feature of the S-PLUS survey, and might represent an opportunity to conduct statistical analysis where photo-z precision and cosmological volume is required, such as luminosity or mass functions.

4 PROBABILITY DENSITY FUNCTIONS

As stressed in Rau et al. (2015), in order to enter the era of precision cosmology (Albrecht et al. 2006), one must be able to incorporate the uncertainty in the redshift estimate into any cosmological analysis. This statement highlights the importance of stop treating photometric redshifts as simple point-estimates and start thinking of them as multi-dimensional PDFs.

As emphasized in Section 3.1, when we introduced the BPZ2 code, in this work we have computed the full PDF in a bi-dimensional redshift-spectral-type space, for every source detected in our images. Similar to what we did in Section 3.4 to evaluate the performance of our photo-z estimates as if they were simple point-estimates, in this section we instead make use of the entire PDFs in both redshift and spectral-type space. Nowadays, there are an increasing number of works where it is emphasized not only the benefit of treating photometric redshift estimates as PDFs rather than as simple point-estimates, but also giving recipes about how to characterize the reliability of these distributions encoding photo-z uncertainties along with different approaches to compensate underestimated (or overestimated) PDFs (Benítez 2000; Fernández-Soto et al. 2002; Coe et al. 2006; Mandelbaum et al. 2008; Cunha et al. 2009; Pelló et al. 2009; Wittman 2009; Bordoloi et al. 2010; Abrahamse et al. 2011; Sheldon et al. 2012; Carrasco Kind & Brunner 2013; Molino et al. 2014; Carrasco Kind & Brunner 2014a; Carrasco Kind & Brunner 2014b; López-Sanjuan et al. 2015; Viironen et al. 2015; López-Sanjuan et al. 2017; Molino et al. 2019; Gomes et al. 2018, among others)

The analytical tools needed to characterize the performance of these distribution functions differ from those previously utilized in Section 3.4. Through the following section, we introduce and utilize a number of approaches to quantify the reliability of our PDFs estimations using the BPZ2, encoding the real photo-z uncertainties.

4.1 Measuring Confidence Levels

We measure the reliability of our PDFs encoding real uncertainties in photometric redshift estimates using the Highest Probability Density (HPD) technique, as described in Wittman et al. (2016). This statistical method is based on the Quantile-Quantile (Q-Q) plots, where the distribution of threshold credible intervals, C , is calculated from a spectroscopic redshift sample. This approach assumes that if PDFs properly represent the redshift uncertainty, the expected distribution of C values should be constant between 0 and 1, with the cumulative distribution function $\hat{F}(C)$ (or CDF) following a 1:1 relation as in a quantile-quantile plot (Q-Q). This technique, which has been implemented in a number of works (i.e., Freeman et al. (2017), Leistedt & Hogg (2017), Cavuoti et al. (2017), Gomes et al. (2018) or Duncan et al. (2018), among others), has proven to be very efficient in describing over- or under-confidence. For example, stressing whether a PDF departs from Gaussianity due to the presence of heavier tails or a larger skew. In addition, we also investigate an optimization Kernel to calibrate our PDFs. This analysis is divided in four categories: magnitude, redshift, spectral-type and Odds.

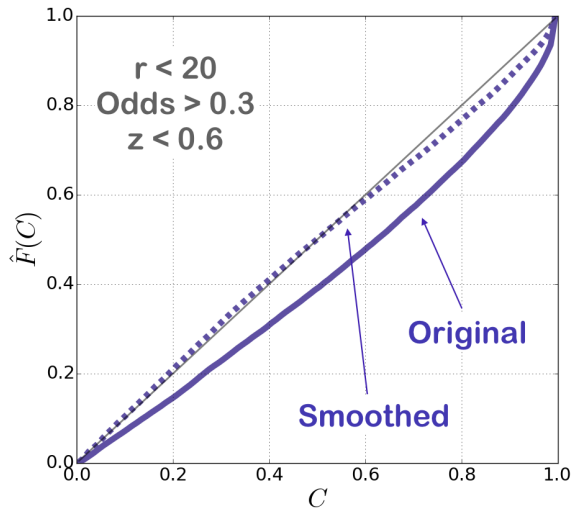


Figure 12. We measure the reliability of our PDFs encoding real uncertainties using the Highest Probability Density (HPD) technique. We recommend to apply a smoothing Gaussian-Kernel of equivalent width $\sigma_{GK}=0.019$ to our PDFs, in order to avoid possible under-estimation effects.

To understand the reliability of our PDFs for all types of galaxies in our catalogs, we divide the spectroscopic redshift sample in multiple intervals: in magnitude bins ($r < 17$, $r < 18$, $r < 19$, $r < 20$ and $r < 21$), in redshift bins ($z < 0.1$, $0.1 < z < 0.2$, $0.2 < z < 0.3$, $0.3 < z < 0.4$ and $0.4 < z < 0.5$), in Odds bins (Odds>0.0, Odds>0.3, Odds>0.6 and Odds>0.9) and in spectral-types (separating our SED models in Early- and Late-types). We explore the dependence of the $\hat{F}(C)$ function as a function of each of the before-mentioned bins. According to the HDP test, we find that our PDFs are systematically underestimated, with a deviation larger the brighter the galaxy, the lower the redshift and the lower the Odds value. Likewise, we find that late-type galaxies show a larger deviation than early-types.

In order to compensate this bias, we look for an optimal Gaussian Kernel (σ_{GK}) to be convolved with our raw PDFs to bring them to the desired 1-to-1 line. In this exercise we explore a range of values from $0.005 < \sigma_{GK} < 0.03$. Although it would be ideal to apply an optimal GK to each individual galaxy according to its magnitude, redshift, Odds value and most likely spectral-type, this approach is computationally expensive. Instead, we prefer to adopt a simpler approach, defining a unique Gaussian Kernel which represents a good compromise between accuracy and simplicity. After a careful examination of the aforementioned parameter space, we recommend to apply a $\sigma_{GK}=0.018$ to our PDFs. As shown in Figure 12, this GK will assure that most galaxies with good photometric redshift estimates in our catalogs (i.e., those with a magnitude $r < 20$, a redshift $z < 0.6$ and Odds>0.3) will have reliable PDFs for statistical analysis.

4.2 Encoding photometric uncertainties (II).

In this Section, we present a complementary discussion about the reliability of the PDFs encoding photometric-z

uncertainties. We compare the error distribution functions obtained from our photometric redshift estimates (see Section 3.3), when they are treated as single-point estimates or as probability distribution functions (i.e., PDFs). In the latter case, before the stacking it is necessary to normalize individual PDFs and subtract the spectroscopic redshift value from each galaxy. We do not separate here galaxies by their spectral-types. As in previous analysis, we divide our spectroscopic redshift galaxy sample in three different Odds bins. We also select galaxies with magnitudes $16 < r < 21$ to assure a well-behaved photometry avoiding very bright and very faint sources. As seen in Figure 13, where the error distribution from point estimates is represented in red and that from the stacked PDFs in blue, both distributions are in good agreement. As expected, galaxies with low Odds values (e.g., left panel) tend to show larger tails than those from point-like estimates. The excess signal comes from secondary peaks in the distribution functions; information ignored by single-point estimates. Galaxies with higher Odds values (e.g., intermediate and right panel), show narrow distribution with little excess in the wings. This effect reflects the fact PDFs for galaxies with high Odds are mostly described by single-peak distributions.

4.3 Reliability mapping the $n(z)$

As explained in Section 4, the BPZ2 code computes a bi-dimensional redshift vs spectral-type probability distribution function for every source in our catalogs. By means of a simple marginalization over the spectral-type information, these bi-dimensional distributions can be collapsed into a single 1-dimensional distribution (i.e., redshift) space that we named here as zPDF. These distribution functions need to satisfy the following normalization criteria to preserve its dimensionality:

$$zPDF_i = \int_T p_i(z, T|D) dT = \int_z p_i(z|D) dz = 1 \quad (5)$$

where $p_i(z, T|D)$ represents the probability distribution function in both redshift (z) and spectral-type (T) space for the i th-galaxy and $p_i(z|D)$ the collapsed probability distribution function in redshift after marginalize over templates.

In this section, we briefly illustrate the capability of our PDFs retrieving the redshift distribution of galaxies (i.e., $n(z)$) in the nearby Universe. We refer the interested reader to López-Sanjuan et al., (in prep.) for an in-depth discussion on the subject. To do so, we compute the PDF-based redshift distribution for all the galaxies with a spectroscopic redshift value lower than $z < 0.5$ and a Odds value ≥ 0.9 , to select galaxies with very secure photometric redshifts in the nearby Universe. The so-selected sample is further divided in three magnitude bins (i.e., $r < 16$, $r < 18$, $r < 21$), to figure the performance of these distributions with the magnitude of sources. For the sake of simplicity, we have preferred not to split the sample according to their spectral-type classification (e.g., among red/blue galaxies) but treating it as a single population. Finally, a redshift resolution of $\Delta z=0.01$ has been adopted to facilitate its visualization. In Figure 14 we compare the PDF-based photometric redshift distribution (red) with the spectroscopic redshift one (blue). As seen

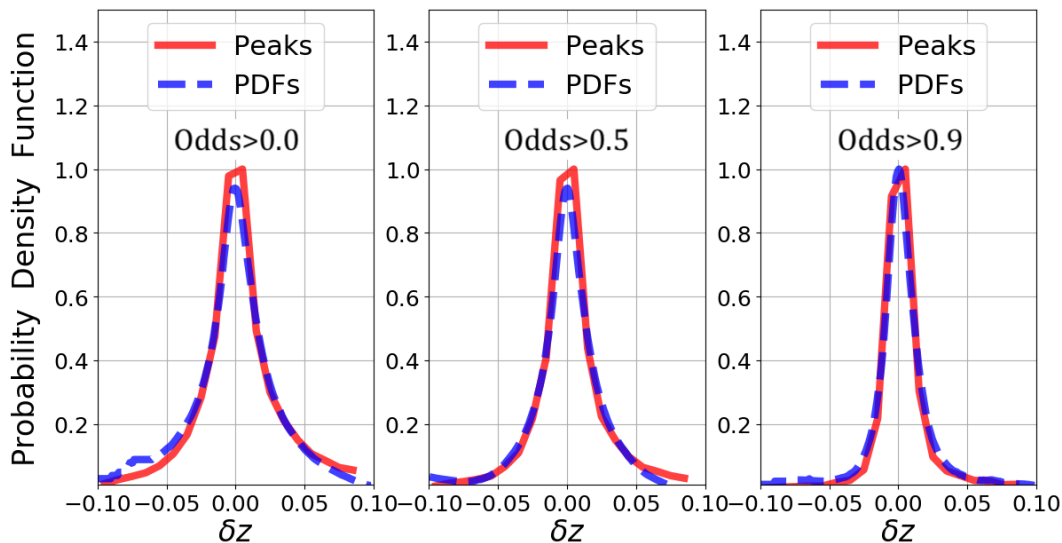


Figure 13. In this figure we show the reliability of the PDFs encoding the photometric redshift uncertainties. From left to right, the distribution correspond to galaxies with magnitude $r < 21$ and Odds > 0.0 , Odds > 0.5 & Odds > 0.9 .

from this figure, our $zPDF$ can successfully retrieve the real distribution of galaxies in the nearby Universe; opening the possibility of revisiting the redshift distribution of galaxies in the nearby Universe down to a magnitudes $r < 21$.

4.4 PDFs for stellar-sources

The S-PLUS photometric catalog includes a Machine Learning-based statistical star/galaxy classification, computed using colours and apparent morphology from sources (Costa-Duarte et al., (in prep.)). Due to the statistical nature of this methodology, every single source in our catalog has been associated with a probability of being a star or a galaxy (see Sampedro et al., (in prep.) for more details). Therefore, the BPZ2 code is run on every detected source independently of its true nature. In this section, we investigate how stars misclassified as being galaxies may contaminate extragalactic analysis. In particular, we tackle this issue by making use of the redshift Probability Distribution Function (i.e., $zPDF$) of sources, since these distributions are further recommended for large statistical analysis since they encode more information from sources that classical point-estimates (see López-Sanjuan et al. (2017) for a longer discussion).

In order to understand how the $zPDF$ of misclassified stars may look like, we did the following exercise. We cross-matched the SDSS/S82 stellar catalog (Ivezić et al. (2007)) with our observations, finding $\sim 250k$ stars down to a magnitude r -band = 21. On these sources, we run the BPZ2 code using the S-PLUS multi-band photometry and derive the corresponding $zPDF$. Finally, we stacked and normalized the final distribution which we named as “Stellar-PDF”. As illustrated in Figure 15, there exists several redshift windows at which photometric redshift estimates for stellar sources tend to cluster. As expected, the most prominent peak sits at redshift $z=0.0$ but there are other secondary peaks at $z=0.008$, $z=0.17$, $z=0.31$, $z=0.50$, $z=0.61$ and $z=0.75$, among others.

Therefore, these regions are more sensitive to include misclassified stars (as galaxies), contaminating any extragalactic analysis. Interestingly, the redshift window described in Section 3.8 (i.e., $0.26 < z < 0.32$), show a minimum in the Stellar-PDF, reassuring the usability of this redshift interval for scientific studies.

5 ABSOLUTE MAGNITUDES AND STELLAR MASSES.

Through this section, we describe how Absolute Magnitudes (§5.1) and Stellar Masses (§5.2) have been estimated for our galaxies, and how photometric redshift uncertainties may affect the estimation of those quantities.

5.1 Absolute Magnitudes.

We use the BPZ2 code to compute the Absolute Magnitudes in the r -band for all sources, according to the most likely redshift and spectral-type, based on the S-PLUS multi-band photometry. These estimates include a template-dependent K-correction described in Table A5. In order to understand the quality of our estimates, we study the impact of the photometric redshift uncertainties when deriving Absolute Magnitudes. To do so, initially we force BPZ2 to use the spectroscopic redshift value for each galaxy previous to the computation of the absolute magnitude. Redshifting the SED models to the exact redshift of each individual galaxy, letting BPZ2 just to look for the model that best fits the data, renders possible to minimize the uncertainties over the spectral-type classification; i.e., breaking down the colour-redshift degeneracy. After BPZ2 finds the best template, it computes the corresponding Absolute Magnitude. As stated before, the comparison of both distributions (i.e., the one using spectroscopic and the one using photometric redshifts)

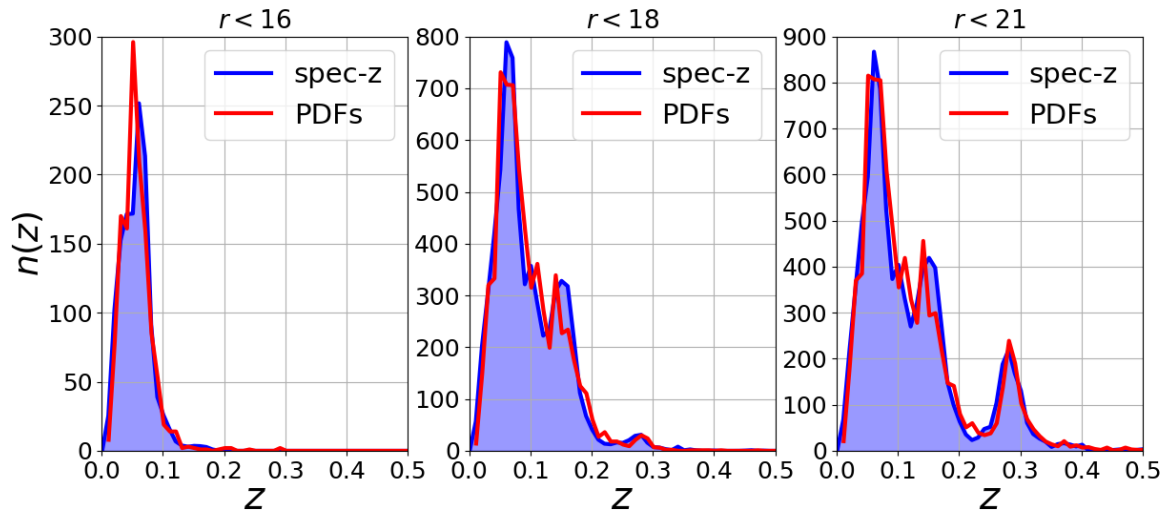


Figure 14. Comparison between the spectroscopic redshift distribution (blue) and the stacked photo-z PDF (red), for a sample of galaxies with Odds ≥ 0.9 and magnitudes $r < 16$, $r < 18$, $r < 21$. A redshift resolution $\Delta z = 0.01$ is adopted to facilitate its visualization.

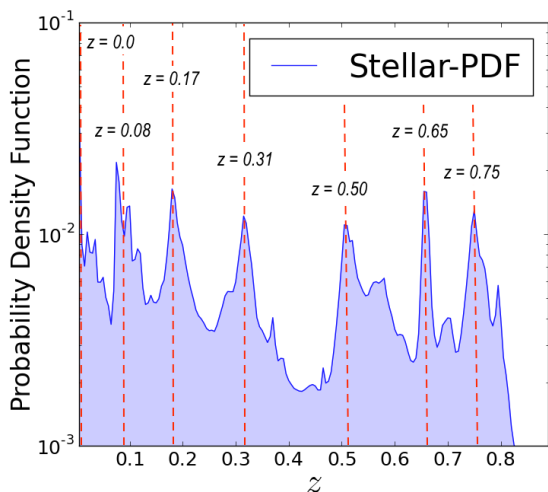


Figure 15. Redshift Probability Density Function (zPDF) for stellar sources. The figure shows the regions where misclassified galactic sources as galaxies may contaminate the most photometric redshift distributions.

serves to quantify the impact of redshift uncertainties when computing absolute magnitudes for all galaxies in the S-PLUS catalogs. In Figure 16, we show the redshift versus absolute magnitude in the r -band (i.e., M_r) for the sample of spectroscopic galaxies presented in Section 2.4. As indicated by the vertical label, the spectral-type of galaxies has been colour-coded; where early-type galaxies appear with red colours and late-type galaxies with blue ones. As expected, the most luminous galaxies in our spectroscopic sample correspond to Luminous Red Galaxies (i.e., LRGs), which start dominating the sample at a redshift $z > 0.4$. Inner panel shows the error distribution observed when computing the Absolute Magnitudes with and without fixing the redshift of galaxies, which has a typical $1-\sigma$ dispersion of RMS = 0.5 magnitudes. Table A5 includes a complete

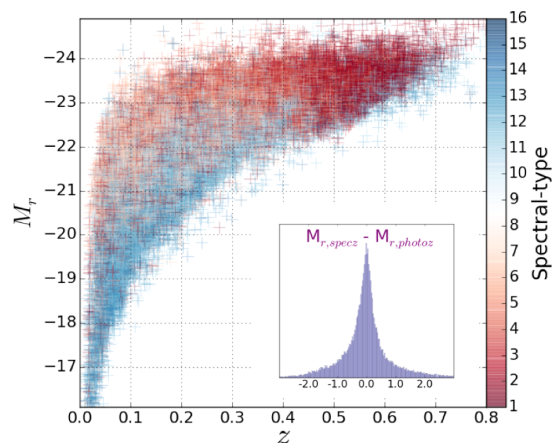


Figure 16. Absolute Magnitude (M_r) versus redshift for galaxies detected in the Stripe-82, according to BPZ2 code. The most likely spectral-type of galaxies is colour coded as indicated by the vertical colour-bar. Inner panel shows the logarithmic error distribution observed when computing the Absolute Magnitudes with and without fixing the redshift of galaxies, which has a typical $1-\sigma$ dispersion of RMS = 0.5 magnitudes.

description of k -corrections which have been performed by the BPZ2 code.

5.2 Stellar-Mass.

We rely on the BPZ2 code to compute stellar masses which uses a mass-to-light empirical relation derived from a colour-magnitude relation similar to that presented in Taylor et al. (2011) for the GAMA survey¹², however refined by López-Sanjuan et al. (2018) based on the ALHAMBRA survey^{13,14}

¹² <http://www.gama-survey.org>

¹³ <http://www.alhambraobservatory.com>

¹⁴ <http://cosmo.iaa.es/content/ALHAMBRA-Gold-catalog>

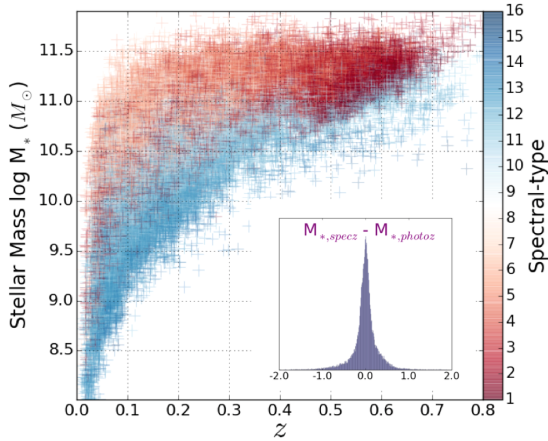


Figure 17. Stellar-Mass (M_*) versus redshift for galaxies detected in the Stripe-82, according to BPZ2 code. The most likely spectral-type of galaxies is colour coded as indicated by the vertical colour-bar. Inner panel shows the logarithmic error distribution observed when computing the stellar-mass with and without fixing the redshift of galaxies, which has a typical $1\text{-}\sigma$ dispersion of $\text{RMS} = 0.1$ magnitudes.

data. According to the authors, the expected uncertainty in these estimates is of the order of $\sigma=0.02\text{dex}$ for red galaxies and $\sigma=0.06\text{dex}$ for late-type galaxies. For the sake of simplicity, here we include the mass-to-light relations (i.e., presented in the aforementioned paper) for red/early-type (Eq. 6) and for blue/late-type galaxies (Eq. 7):

$$\log(M_\odot/L_i)_r = 1.02 + 0.84 \times (g - i) \quad (6)$$

$$\log(M_\odot/L_i)_b = 1.41 + 0.21 \times (g - i) + 0.14 \times (g - i)^2 \quad (7)$$

As in the previous section, we study the impact of the photometric redshift uncertainties when computing stellar-masses and compare our results with those from the literature. In Figure 17, we show the redshift versus stellar-mass (i.e., M_*) for the sample of spectroscopic galaxies presented in Section 2.4. As indicated by the vertical label, the spectral-type of galaxies has been colour-coded; where early-type galaxies appear with red colours and late-type galaxies with blue ones. As expected, the most luminous galaxies in our spectroscopic sample correspond to Luminous Red Galaxies (i.e., LRGs), which start dominating the sample at a redshift $z > 0.4$. Inner panel shows the logarithmic error distribution observed when computing the stellar-mass with and without fixing the redshift of galaxies, which has a typical $1\text{-}\sigma$ dispersion of $\text{RMS} = 0.1$ magnitudes.

6 TESTING THE S-PLUS PHOTOMETRY.

In this section, we present a number of tests aiming at validating the quality of our photometric catalogs. Initially, in Section 6.1, we use the spectroscopic redshift sample to check the quality of the photometric zero-point estimates.

Finally, in Section 6.2, we take advantage of using a SED-fitting based photo-z code to characterize the accuracy of the photometric uncertainties provided for sources in our catalogs.

6.1 Photometric ZP-offsets

As explained in Section 3.1, one of the advantages of running SED-fitting based photometric redshift codes on a sample of galaxies with spectroscopic redshift information is the possibility of making comparisons between the observed and the predicted colours of galaxies. These comparisons serve to a double purpose. When these quantities are computed from a large sample of heterogeneous galaxies at different magnitudes and redshifts, it becomes possible to flag systematic zero-point offsets coming from the initial photometric calibrations. As demonstrated in many works (e.g., Coe et al. 2006, Jouvel et al. 2014, Molino et al. 2014) these corrections may enhance the overall photometric redshift precision since they improve the agreement between data and models. Likewise, when these differences are represented as a function of the magnitude (or the signal-to-noise) for each individual band, these error distributions may warn about systematics related to the PSF-homogenization across filters or issues with the electronic response of the CCD camera.

Based on the aforementioned ideas, we utilized the spectroscopic redshift sample presented in Section 2.4, to look for potential systematics in the S-PLUS multi-band photometry (Sampedro et al., (in prep.)). Since the S-PLUS/Stripe-82 observations are made of 170 different pointings, the calibration process is first run individually in each field and then combined into a final averaged value. Initially, we start by comparing the so-derived zero-point corrections as a function of wavelength (i.e., filters). The results from this exercise are illustrated in Figure 18. We find small deviations in every filter, smaller than a few hundredth of a magnitude. Interestingly, except for the fourth and twelfth filter, the intrinsic dispersion is always larger than the corrections. This fact makes it complicated to assure these offsets correspond to real issues in the photometry more than to the intrinsic photometric dispersion of galaxy colours due to the noise. The observed zero-point corrections are noted down in Table 1.

Later on, we represent these zero-point corrections as a function of the magnitude. In this case, we look for systematics in the way the photometry is performed. As before, we combine the results from the 170 individual fields. Figure 19 shows an example of the observed differences between predicted and observed colours as a function of the r-band magnitude. Internal red line corresponds to the average value binned in bins of $\delta m = 0.1$ magnitudes. This result proves that there seem not to be any dependence with the magnitude (or surface brightness), assuring that the photometry is robust even for faint sources.

6.2 Photometric-noise check.

Following the same philosophy as in the previous section, we take advantage of our SED-fitting based photo-z algorithm to check the level of agreement (or disagreement) between

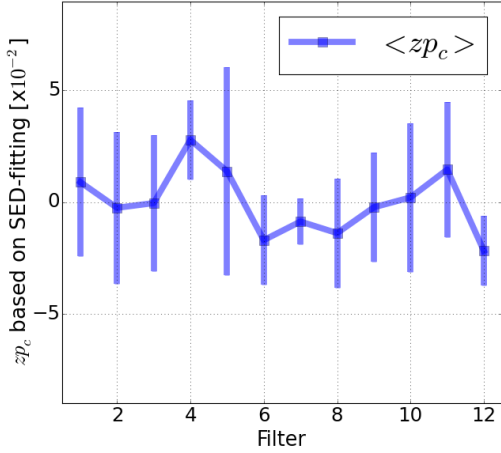


Figure 18. The figure shows the computed ZP-corrections to our photometry according to BPZ2, based on the spectroscopic redshift sample.

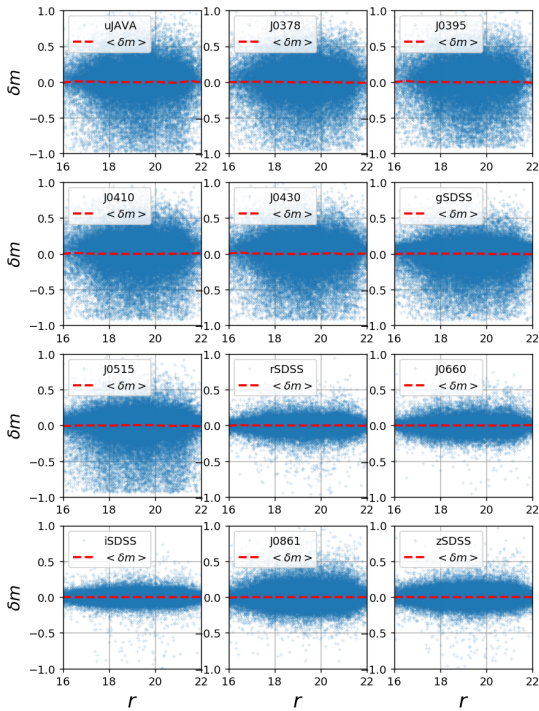


Figure 19. Comparison between the observed and the expected magnitudes as a function of the r-band magnitude. Internal red lines correspond to the average value binned in magnitude bins of $\delta m = 0.1$. These distributions correspond to the global values for each filter averaged over all independent fields making up the S-PLUS/Stripe-82 catalog. No systematic is observed neither for bright nor for faint sources, assuring the reliability of the S-PLUS photometry.

Table 1. S-PLUS Photometric re-calibration. The table summarizes the main photometric zero-point refinements derived with the BPZ2 using galaxies with spectroscopic redshift. It includes the filter name (*Filter*), the average zero-point corrections ($\langle ZP_{off} \rangle$) and average zero-point dispersion (σ_{ZP}^{off}).

Filter	$\langle ZP_{off} \rangle$	σ_{ZP}^{off}
(1) uJAVA	0.009	0.033
(2) J0378	0.002	0.034
(3) J0395	0.000	0.030
(4) J0410	0.028	0.018
(5) J0430	0.014	0.045
(6) gSDSS	-0.017	0.020
(7) J0515	-0.009	0.010
(8) rSDSS	-0.014	0.024
(9) J0660	-0.002	0.024
(10) iSDSS	0.002	0.033
(11) J0861	0.014	0.030
(12) zSDSS	-0.022	0.016

the reported photometric noise of sources in our catalogs and the average differences between observed and predicted colours. This exercise serves to understand if there might be additional sources of uncertainties in our photometry, than those already flagged and corrected in the S-PLUS photometric pipeline.

In Figure 20 we show, for every individual filter, the error distribution between the expected and observed colours (i.e., δ_m) for the spectroscopic redshift galaxy sample (gray histogram), together with the global photometric error distribution (red dashed line). The latter is calculated as the square root of the quadratic sum of Gaussian functions of width the reported photometric noise of every detection in a given filter. These distributions correspond to global values averaged over the 170 independent fields and sources with magnitudes $14 < r < 19$. This analysis serves to demonstrate that, after recalibrating the photometric noise of images, the photometric uncertainties reported for each detection match the observed dispersion between data and models computed during the SED-fitting procedure. Interestingly, we notice that several filters (e.g., *uJava*, *J0515*, *J0861*) show extended tails, sometimes asymmetric, which cannot be explained by regular Poisson noise. This excess signal may arise from additional sources of uncertainties not reported during the image reduction and photometry extraction.

6.3 Photometric Completeness matrices.

In order to be able to compute the redshift distribution of galaxies in the Stripe-82 region (Azanha et al., in prep.), it is necessary to previously derive the expected completeness function of our observations; as much as a function of the magnitude as the redshift. These estimates will serve to compensate the apparent (observed) number counts in our catalogs due to the limited depth of our observations.

As motivated in Section 2.4, we can take advantage of the photometric depth of the spectroscopic redshift sample of galaxies in the Stripe-82 to carry out this exercise, since it has a similar photometric depth to that of our observations. Despite the fact the spectroscopic redshift sample utilized in this work is by no means complete in magnitude and redshift

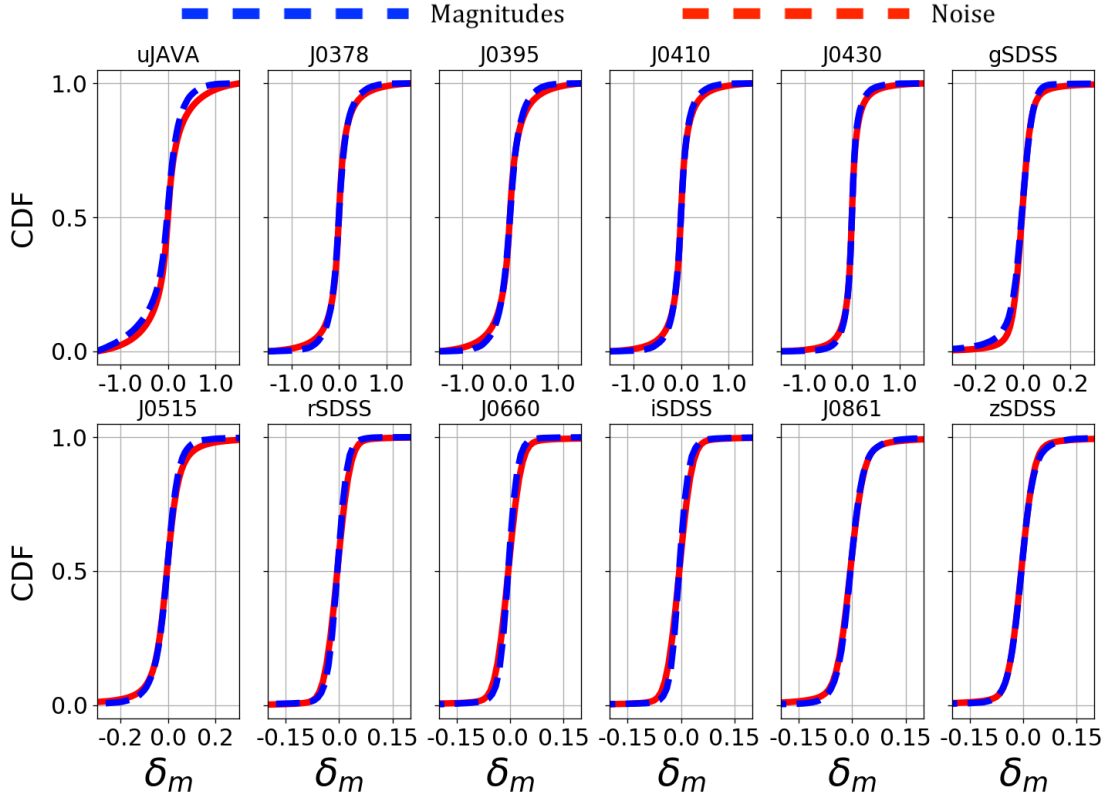


Figure 20. The figure shows, for every individual filter, the error distribution between the expected and observed colours (i.e., δ_m) for the spectroscopic redshift galaxy sample (gray histogram), together with the global photometric error distribution (red dashed line). These distributions correspond to global values averaged over the 90 independent fields and sources with magnitudes $14 < r < 19$.

(i.e., it does not include all galaxies in the Stripe-82 area), it does contain a large number of galaxies at faint magnitudes and high redshift ranges. Therefore, it may give us a first order characterization of the expected incompleteness at different redshift/magnitude ranges. These completeness functions will be improved in the future once the S-PLUS survey has covered other sky regions with deeper spectroscopic redshift samples such as VVDS (Le Fèvre et al. 2004) or DEEP2 (Newman et al. 2013). In order to improve the characterization of our selection functions, we have split the spectroscopic redshift sample among early and late-type galaxies, where this classification is based on the most likely spectral-type for each galaxy according to BPZ2 code.

As seen in Figure 21, we define a magnitude-redshift grid where, for each interval, we calculate the fraction of galaxies with spectroscopic redshifts that were also detected in our images. This computation needs to take into account solely common areas, i.e., to differentiate between not detected (i.e., below the detection threshold) from non-observed (i.e., outside the S-PLUS footprint). The so-computed matrix can be converted into a 1-dimensional array where the redshift completeness is computed for sources within a certain magnitude bin. In short, we observe that our observations might be fairly complete up to a redshift $z < 0.5$ and down to a magnitude $r < 20$, for both early- and late-type galaxies.

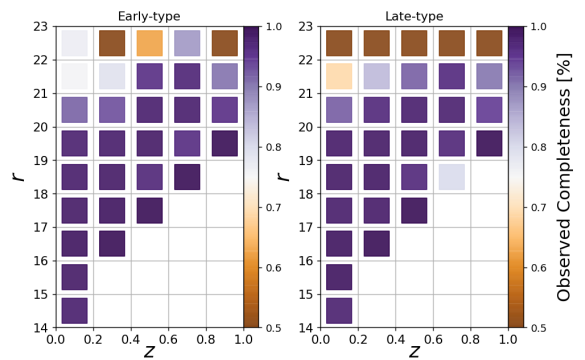


Figure 21. Photometric Redshift Completeness for our observations. The fraction of detected spectroscopic galaxies, as a function of the magnitude (r) and redshift (z), is colour-coded as indicated by the vertical colorbar.

7 SUGGESTIONS ON HOW TO HANDLE THE S-PLUS PHOTO-Z

In order to help users retrieving more reliable samples of galaxies for their science cases, here we include a number of suggestions:

- Multi-band Photometric catalogs include a Photometric-Quality Flag (based on the `SExtractor` code), which can be used to exclude objects subject to

have a compromised photometry. Sources with very bright nearby objects (i.e., such as saturated stars), might be either removed from the analysis or, in case of necessity, to adopt the smallest apertures to guarantee a high signal-to-noise measurement.

- The BPZ2 code provides a redshift estimate for every source in the catalog, irrespectively of its true nature. In order to decontaminate galaxy samples from galactic sources, we recommend either to adopt a rigorous selection criteria such as the one presented in [Costa-Duarte et al., \(in prep.\)](#), or to treat sources in a flexible statistical framework, where the contribution of each detection to a given analysis is weighted according to the probabilities of being a star or a galaxy.

- In order to select a clean and reliable galaxy sample, we encourage the user to use the `Odds` parameter. Information displayed in [Table A2](#), may help understanding the selection criteria required for a given analysis in terms of photometric redshift error, bias or contamination.

- Sources with relatively high χ^2 values from the SED-fitting analysis might be treated with care. These sources may represent either objects with faulty photometry or with a SED different from those considered in this work.

- Although BPZ2 provides the most likely redshift and a confident redshift interval for each galaxy, it is worth stressing that most galaxies show several solutions compatible with the photometric data. Typically, these secondary peaks in redshift correspond to galaxies with different spectral-types. Therefore, we encourage the users not to treat photometric redshifts as simple point-estimates but rather as a multidimensional distribution functions.

8 DATA ACCESS

The S-PLUS multi-band photometric catalogs, including photometric redshift estimates, redshift Probability Distribution Functions, Completeness functions and k -corrections, along with other additional value-added products, such as stellar-mass content and absolute magnitudes for galaxies and a star/galaxy classification, can be accessed through the following url: <https://datalab.noao.edu/splus/>.

9 SUMMARY

In this work, we make use of the Data Release 1 (DR1) and the well-tested Bayesian Photometric Redshift (BPZ2) code to compute and characterize the expected precision of the S-PLUS photometric redshifts. The public photometric catalogue utilized for this exercise corresponds to a nominal area of 336 deg^2 along the Stripe-82, divided in 170 individual and contiguous pointings, observed with a 5 broad + 7 narrow-band photometric passbands, with a typical photometric depth of $r = 21$ (AB) magnitudes. The catalogue (presented in previous papers), includes up to $\sim 3\text{M}$ detected sources, where $1/3$ has been classified as potential extragalactic sources. Besides, we take advantage of the abundant spectroscopic redshift information available in this sky region, to compile a large and suitable control sample of ~ 100.000 galaxies with known spectroscopic redshifts, down

to a magnitude $r = 22$ and up to a redshift $z = 1$, to compare our estimates with.

In order to facilitate their interpretation, the results of this comparison are expressed in terms of basic astronomical variables such as the r -band magnitude, the redshift or the spectral-type of galaxies, and the BPZ2 `Odds` parameter. Although there is an in-depth description of our findings in the Appendix section, here we outline several results. We find a photometric redshift precision of $\sigma_z \leq 0.8\%$ or $\sigma_z \leq 2.0\%$ for galaxies with magnitudes $r < 17$ and $r < 19$, respectively. Similarly, a precision of $\sigma_z \leq 1.5\%$ and $\sigma_z \leq 3.0\%$ is found for galaxies with a redshift $z < 0.05$ and $z < 0.5$, respectively. Interestingly, early-type galaxies at $z < 0.1$ and $z < 0.5$ reach a precision of $\sigma_z \leq 1.0\%$ and $\sigma_z \leq 2.0\%$. Likewise, we find a precision of $\sigma_z \leq 0.8\%$ and $\sigma_z \leq 1.5\%$ for galaxies with values `Odds` > 0.9 and `Odds` > 0.6 , respectively. The brightest early-type galaxies in our catalogue reach a superb precision of $\sigma_z \leq 0.6\%$. In all the aforementioned cases, our photo- z estimates show a negligible bias (μ_z) and a fraction of catastrophic outliers (η) inferior to 1%. Based on these results, we forecast a total of $\sim 2\text{M}$ galaxies with a precision $\sigma_z \leq 0.01$ or 16M galaxies with a $\sigma_z \leq 0.02$, in the S-PLUS survey once the entire footprint is observed.

We identify a redshift window ($0.26 < z < 0.32$) where our photometric redshift estimates double its precision, due to the simultaneous detection of both [OIII] and H α emission-lines in the $J0660$ & $J0861$ narrow-band filters. This fact brings a window opportunity in S-PLUS to conduct statistical studies such as luminosity functions, given the powerful combination of both photometric redshift precision and cosmological volume surveyed at that redshift depth.

In order to fully exploit the information provided by our multi-band photometry, besides these point-like estimates, in this work we also compute the full Probability Distribution Function (i.e., PDF) provided by the BPZ2 code for each detection. As demonstrated in this work, these bi-dimensional (i.e., redshift-spectral-type) distributions can successfully encode statistically the redshift uncertainties, and be used to recover the galaxy redshift distribution of galaxies at $z < 0.4$, with unprecedented precision for a photometric survey in the Southern hemisphere.

In the final sections of this work, an effort is devoted to double-check the quality of the input photometry, finding no systematic effects such as substantial zero-point corrections or aperture effects. The comparison of expected and observed colours for galaxies with known redshifts indicates that photometric uncertainties in catalogues are properly calibrated. Finally, in order to help deriving statistical analysis in the S-PLUS survey, an effort is made to characterize the photometric completeness of the survey in terms of both r -band magnitude and redshift. These and other complementary materials are available online.

10 ACKNOWLEDGMENT

AMB would like to acknowledge the financial support of the Brazilian funding agency FAPESP (Post-doc fellowship - process number 2014/11806-9), and his colleague Dr. Carlos

López-Sanjuan for all his valuable advices regarding PDF analysis. Likewise, AMB acknowledges Ulisses Manzo and Carlos E. Paladini at IAG/USP for helping with software installation. In addition, AMB would like to dedicate this work to his first son Tiago who was born in Brazil during the time this paper was written. MVCD thanks his scholarship from FAPESP (processes 2014/18632-6 and 2016/05254-9). This work has made use of the computing facilities of the Laboratory of Astroinformatics (IAG/USP, NAT/Unicisul), whose purchase was made possible by the Brazilian agency FAPESP (grant 2009/54006-4) and the INCT-A. The S-PLUS project, including the T80S robotic telescope and the S-PLUS scientific survey, was founded as a partnership between the Fundação de Amparo a Pesquisa do Estado de São Paulo (FAPESP), the Observatório Nacional (ON), the Federal University of Sergipe (UFS), and the Federal University of Santa Catarina (UFSC), with important financial and practical contributions from other collaborating institutes in Brazil, Chile (Universidad de La Serena), and Spain (Centro de Estudios de Física del Cosmos de Aragón, CE-FCA). LSJ acknowledges support from FAPESP and CNPq. JLNC is grateful for financial support received from the GRANT PROGRAMS FA9550-15-1-0167 and FA9550-18-1-0018 of the Southern Office of Aerospace Research and development (SOARD), a branch of the Air Force Office of the Scientific Research International Office of the United States (AFOSR/IO). ADMD thanks FAPESP for financial support. SA acknowledges financial support from Conselho Nacional de Desenvolvimento Científico e Tecnológico (CNPq, grant 454794/2015-0). AAC acknowledges support from FAPERJ (grant E26/203.186/2016) and CNPq (grants 304971/2016-2 and 401669/2016-5). L.A.A. would like to acknowledge the financial support from FAPESP (N 2012/09716-6, 2013/18245-0). ACS acknowledges funding from CNPq (403580/2016-1, 311153/2018-6) and FAPERGS (17/2551-0001). J. A. H. J. thanks to Brazilian institution CNPq for financial support through postdoctoral fellowship (project 150237/2017-0) and Chilean institution CONICYT, Programa de Astronomía, Fondo ALMA-CONICYT 2017, Código de proyecto 31170038. PAAL thanks the support of CNPq, grant 309398/2018-5.

REFERENCES

- Abazajian K. N., et al., 2009, *ApJS*, **182**, 543
 Abolfathi B., et al., 2018, *ApJS*, **235**, 42
 Abrahamse A., Knox L., Schmidt S., Thorman P., Tyson J. A., Zhan H., 2011, *ApJ*, **734**, 36
 Alam S., et al., 2015, *ApJS*, **219**, 12
 Albareti F. D., et al., 2017, *ApJS*, **233**, 25
 Albrecht A., et al., 2006, *ArXiv Astrophysics e-prints*,
 Annis J., et al., 2014, *ApJ*, **794**, 120
 Arenou F., et al., 2017, *A&A*, **599**
 Arnouts S., et al., 2002, *MNRAS*, **329**, 355
 Asboth V., et al., 2016, *MNRAS*, **462**, 1989
 Ascaso B., Mei S., Benítez N., 2015, *MNRAS*, **453**, 2515
 Ascaso B., et al., 2016, *MNRAS*, **456**, 4291
 Assef R. J., et al., 2008, *ApJ*, **676**, 286
 Assef R. J., et al., 2010, *ApJ*, **713**, 970
 Babbedge T. S. R., et al., 2004, *MNRAS*, **353**, 654
 Bailer-Jones C. A. L., 2004, *A&A*, **419**, 385
 Ball N. M., Brunner R. J., Myers A. D., Strand N. E., Alberts S. L., Tchong D., 2008, *ApJ*, **683**, 12
 Baum W. A., 1962, in *McVittie G. C., ed., IAU Symposium Vol. 15, Problems of Extra-Galactic Research*. p. 390
 Beckwith S. V. W., et al., 2006, *AJ*, **132**, 1729
 Benítez N., 2000, *ApJ*, **536**, 571
 Benítez N., et al., 2009a, *ApJ*, **691**, 241
 Benítez N., et al., 2009b, *ApJ*, **692**, L5
 Benítez N., et al., 2014, preprint, ([arXiv:1403.5237](https://arxiv.org/abs/1403.5237))
 Bertin E., 2010a, SCAMP: Automatic Astrometric and Photometric Calibration, Astrophysics Source Code Library (ascl:1010.063)
 Bertin E., 2010b, SWarp: Resampling and Co-adding FITS Images Together, Astrophysics Source Code Library (ascl:1010.068)
 Bertin E., 2013, PSFEx: Point Spread Function Extractor, Astrophysics Source Code Library (ascl:1301.001)
 Bertin E., Arnouts S., 2010, SExtractor: Source Extractor, Astrophysics Source Code Library (ascl:1010.064)
 Bolzonella M., Miralles J.-M., Pelló R., 2000, *A&A*, **363**, 476
 Bonfield D. G., Sun Y., Davey N., Jarvis M. J., Abdalla F. B., Banerji M., Adams R. G., 2010, *MNRAS*, **405**, 987
 Bordoloi R., Lilly S. J., Amara A., 2010, *MNRAS*, **406**, 881
 Brammer G. B., van Dokkum P. G., Coppi P., 2008, *ApJ*, **686**, 1503
 Budavári T., 2009, *ApJ*, **695**, 747
 Bundy K., et al., 2015, *ApJS*, **221**, 15
 Burke D. L., et al., 2018, *AJ*, **155**, 41
 Carrasco Kind M., Brunner R. J., 2013, *MNRAS*, **432**, 1483
 Carrasco Kind M., Brunner R. J., 2014a, *MNRAS*, **438**, 3409
 Carrasco Kind M., Brunner R. J., 2014b, *MNRAS*, **442**, 3380
 Cavuoti S., Amaro V., Brescia M., Vellucci C., Tortora C., Longo G., 2017, *MNRAS*, **465**, 1959
 Cenarro A. J., et al., 2019, *A&A*, **622**, A176
 Coe D., Benítez N., Sánchez S. F., Jee M., Bouwens R., Ford H., 2006, *AJ*, **132**, 926
 Coil A. L., et al., 2011, *ApJ*, **741**, 8
 Colless M., et al., 2001, *MNRAS*, **328**, 1039
 Collister A. A., Lahav O., 2004, *PASP*, **116**, 345
 Connolly A. J., Csabai I., Szalay A. S., Koo D. C., Kron R. G., Munn J. A., 1995, *AJ*, **110**, 2655
 Csabai I., et al., 2003, *AJ*, **125**, 580
 Cunha C. E., Lima M., Oyaizu H., Frieman J., Lin H., 2009, *MNRAS*, **396**, 2379
 Dahlen T., et al., 2010, *ApJ*, **724**, 425
 Dawson K. S., et al., 2013, *AJ*, **145**, 10
 Drinkwater M. J., et al., 2010, *MNRAS*, **401**, 1429
 Drlica-Wagner A., et al., 2018, *ApJS*, **235**, 33
 Duncan K. J., et al., 2018, *MNRAS*, **473**, 2655
 Erben T., et al., 2013, *MNRAS*, **433**, 2545
 Eriksen M., et al., 2018, preprint, ([arXiv:1809.04375](https://arxiv.org/abs/1809.04375))
 Feldmann R., et al., 2006, *MNRAS*, **372**, 565
 Ferguson H., et al., 1995, in *American Astronomical Society Meeting Abstracts*. p. 1294
 Fernández-Soto A., Lanzetta K. M., Yahil A., 1999, *ApJ*, **513**, 34
 Fernández-Soto A., Lanzetta K. M., Chen H.-W., Levine B., Yahata N., 2002, *MNRAS*, **330**, 889
 Firth A. E., Lahav O., Somerville R. S., 2003, *MNRAS*, **339**, 1195
 Fliri J., Trujillo I., 2016, *MNRAS*, **456**, 1359
 Fowler J. W., et al., 2010, *ApJ*, **722**, 1148
 Franzen T. M. O., et al., 2014, *MNRAS*, **439**, 1212
 Freeman P. E., Newman J. A., Lee A. B., Richards J. W., Schafer C. M., 2009, *MNRAS*, **398**, 2012
 Freeman P. E., Izbicki R., Lee A. B., 2017, *MNRAS*, **468**, 4556
 Frieman J. A., et al., 2008, *AJ*, **135**, 338
 Gawiser E., et al., 2006, *ApJS*, **162**, 1
 Geach J. E., et al., 2017, *ApJS*, **231**, 7
 Gerdes D. W., Sypniewski A. J., McKay T. A., Hao J., Weis M. R., Wechsler R. H., Busha M. T., 2010, *ApJ*, **715**, 823

- Gomes Z., Jarvis M. J., Almosallam I. A., Roberts S. J., 2018, *MNRAS*, **475**, 331
- Grogin N. A., et al., 2011, *ApJS*, **197**, 35
- Gruel N., et al., 2012, in *Observatory Operations: Strategies, Processes, and Systems IV*. p. 84481V, doi:10.1117/12.925581
- Heywood I., et al., 2016, *MNRAS*, **460**, 4433
- Hickson P., Mulrooney M. K., 1998, *ApJS*, **115**, 35
- Hickson P., Gibson B. K., Callaghan K. A. S., 1994, *MNRAS*, **267**, 911
- Hildebrandt H., et al., 2010, *A&A*, **523**, A31
- Hodge J. A., Becker R. H., White R. L., Richards G. T., Zeimann G. R., 2011, *AJ*, **142**, 3
- Hsieh B. C., Yee H. K. C., Lin H., Gladders M. D., 2005, *ApJS*, **158**, 161
- Ilbert O., et al., 2006, *A&A*, **457**, 841
- Ilbert O., et al., 2009, *ApJ*, **690**, 1236
- Illingworth G. D., et al., 2013, *ApJS*, **209**, 6
- Ivezic Ž., et al., 2007, *AJ*, **134**, 973
- Ivezic Z., et al., 2008, preprint, (arXiv:0805.2366)
- Jiang L., et al., 2014, *ApJS*, **213**, 12
- Jiménez-Teja Y., Benítez N., Molino A., Fernandes C. A. C., 2015, *MNRAS*, **453**, 1136
- Jones D. H., et al., 2004, *MNRAS*, **355**, 747
- Jordi C., et al., 2006, *MNRAS*, **367**, 290
- Jouvel S., et al., 2014, *A&A*, **562**, A86
- Kaiser N., et al., 2002, in *Tyson J. A., Wolff S., eds, Proc. SPIE Vol. 4836, Survey and Other Telescope Technologies and Discoveries*. pp 154–164, doi:10.1117/12.457365
- Kotulla R., Fritze U., Weibacher P., Anders P., 2009, *MNRAS*, **396**, 462
- LaMassa S. M., et al., 2016, *ApJ*, **817**, 172
- Laurino O., D’Abrusco R., Longo G., Riccio G., 2011, *MNRAS*, **418**, 2165
- Lawrence A., et al., 2007, *MNRAS*, **379**, 1599
- Le Fèvre O., et al., 2004, *A&A*, **428**, 1043
- Le Fèvre O., et al., 2005, *A&A*, **439**, 845
- Leistedt B., Hogg D. W., 2017, *ApJ*, **838**, 5
- Levi M., et al., 2013, preprint, (arXiv:1308.0847)
- López-Sanjuan C., et al., 2015, *A&A*, **576**, A53
- López-Sanjuan C., et al., 2017, *A&A*, **599**, A62
- López-Sanjuan C., et al., 2018, preprint, (arXiv:1805.03609)
- Lotz J. M., et al., 2017, *ApJ*, **837**, 97
- Madau P., 1995, *ApJ*, **441**, 18
- Mandelbaum R., et al., 2008, *MNRAS*, **386**, 781
- Marín-Franch A., et al., 2012, in *Modern Technologies in Space- and Ground-based Telescopes and Instrumentation II*. p. 84503S, doi:10.1117/12.925430
- Marín-Franch A., Taylor K., Cenarro J., Cristóbal-Hornillos D., Moles M., 2015, *IAU General Assembly*, **22**, 2257381
- Martí P., Miquel R., Bauer A., Gaztañaga E., 2014a, *MNRAS*, **437**, 3490
- Martí P., Miquel R., Castander F. J., Gaztañaga E., Eriksen M., Sánchez C., 2014b, *MNRAS*, **442**, 92
- Moles M., et al., 2008, *AJ*, **136**, 1325
- Molino A., et al., 2014, *MNRAS*, **441**, 2891
- Molino A., et al., 2017, *MNRAS*, **470**, 95
- Molino A., et al., 2019, *A&A*, **622**, A178
- Mooley K. P., et al., 2016, *ApJ*, **818**, 105
- Morrissey P., et al., 2007, *ApJS*, **173**, 682
- Newman J. A., et al., 2013, *ApJS*, **208**, 5
- Nieves-Seoane L., et al., 2017, *MNRAS*, **464**, 4331
- Padmanabhan N., et al., 2008, *ApJ*, **674**, 1217
- Papovich C., et al., 2016, *ApJS*, **224**, 28
- Pelló R., et al., 2009, *A&A*, **508**, 1173
- Pérez-González P. G., et al., 2013, *ApJ*, **762**, 46
- Planck Collaboration et al., 2014, *A&A*, **571**, A16
- Postman M., et al., 2012, *ApJS*, **199**, 25
- Rau M. M., Seitz S., Brimioufle F., Frank E., Friedrich O., Gruen D., Hoyle B., 2015, *MNRAS*, **452**, 3710
- Refregier A., Amara A., Kitching T. D., Rassat A., Scaramella R., Weller J., Euclid Imaging Consortium f. t., 2010, preprint, (arXiv:1001.0061)
- Richards G. T., et al., 2001, *AJ*, **122**, 1151
- Richards G. T., et al., 2005, *MNRAS*, **360**, 839
- Sánchez C., et al., 2014, *MNRAS*, **445**, 1482
- Sawicki M. J., Lin H., Yee H. K. C., 1997, in *Tanvir N. R., Aragon-Salamanca A., Wall J. V., eds, The Hubble Space Telescope and the High Redshift Universe*. p. 175 (arXiv:astro-ph/9610027)
- Schlafly E. F., et al., 2012, *ApJ*, **756**, 158
- Schlegel D., White M., Eisenstein D., 2009, in *astro2010: The Astronomy and Astrophysics Decadal Survey*. (arXiv:0902.4680)
- Shanks T., et al., 2015, *MNRAS*, **451**, 4238
- Sheldon E. S., Cunha C. E., Mandelbaum R., Brinkmann J., Weaver B. A., 2012, *ApJS*, **201**, 32
- Soo J. Y. H., et al., 2018, *MNRAS*, **475**, 3613
- Taniguchi Y., et al., 2007, *ApJS*, **172**, 9
- Taylor E. N., et al., 2011, *MNRAS*, **418**, 1587
- The Dark Energy Survey Collaboration et al., 2017, preprint, (arXiv:1712.06209)
- The LSST Dark Energy Science Collaboration et al., 2018, preprint, (arXiv:1809.01669)
- Timlin J. D., et al., 2016, *ApJS*, **225**, 1
- Vanzella E., et al., 2004, *A&A*, **423**, 761
- Viero M. P., et al., 2014, *ApJS*, **210**, 22
- Viironen K., et al., 2015, *A&A*, **576**, A25
- Wadadekar Y., 2005, *PASP*, **117**, 79
- Wang D., Zhang Y. X., Liu C., Zhao Y. H., 2007, *MNRAS*, **382**, 1601
- Way M. J., Foster L. V., Gazis P. R., Srivastava A. N., 2009, *ApJ*, **706**, 623
- Weinstein M. A., et al., 2004, *ApJS*, **155**, 243
- Wittman D., 2009, *ApJ*, **700**, L174
- Wittman D., Bhaskar R., Tobin R., 2016, *MNRAS*, **457**, 4005
- Wolf C., 2009, *MNRAS*, **397**, 520
- Wolf C., et al., 2001, *A&A*, **365**, 681
- Wolf C., Meisenheimer K., Rix H.-W., Borch A., Dye S., Kleinheinrich M., 2003, *A&A*, **401**, 73
- Wright E. L., et al., 2010, *AJ*, **140**, 1868
- York D. G., et al., 2000, *AJ*, **120**, 1579
- Zheng H., Zhang Y., 2012, in *Software and Cyberinfrastructure for Astronomy II*. p. 845134, doi:10.1117/12.925314
- Zheng W., et al., 2012, *Nature*, **489**, 406
- Zitrin A., et al., 2014, *ApJ*, **793**, L12
- de Jong J. T. A., et al., 2015, *A&A*, **582**, A62

¹ Universidade de São Paulo, IAG, Rua do Mato 1225, São Paulo, SP, Brazil

² Departamento de Astronomia, Instituto de Física, Universidade Federal do Rio Grande do Sul (UFRGS), Av. Bento Gonçalves 9500,

³ Instituto de Física, Universidade de São Paulo, Rua do Matão 1371, São Paulo, SP 05508-090, Brazil

⁴ Departamento de Física y Astronomía, Facultad de Ciencias, Universidad de La Serena, Av. Juan Cisternas 1200 Norte, La Serena, Chile.

⁵ Instituto de Investigación Multidisciplinario en Ciencia y Tecnología, Universidad de La Serena. Avenida Juan Cisternas 1400, La Serena, Chile

⁶ NOAO, P.O. Box 26732, Tucson, AZ 85726

⁷ Departamento de Física, Universidade Federal de Santa Catarina, Florianópolis, SC, 88040-900, Brazil

⁸ Departamento de Ciências Físicas, Universidad Andrés Bello, Fernández Concha 700, Las Condes, Santiago, Chile

⁹ Valongo Observatory, Federal University of Rio de Janeiro, Ladeira Pedro Antonio 43, Saude Rio de Janeiro, RJ, 20080-090, Brazil

¹⁰ Instituto de Matemática, Estatística e Física, Universidade Federal do Rio Grande, Rio Grande 96203-900, Brazil

¹¹ Observatório Nacional/MCTIC, Rua Gen. José Cristino, 77, 20921-400, Rio de Janeiro, Brazil

¹² Departamento de Física, Universidade Federal de Sergipe, Av. Marechal Rondon, S/N, 49000-000 São Cristóvão, SE, Brazil

¹³ Center for Space Science and Technology, University of Maryland, Baltimore County, 1000 Hilltop Circle, Baltimore, MD 21250, USA

¹⁴ Center for Earth System Science, National Institute for Space Research, Av. dos Astronautas, 1758, São José dos Campos, Brazil

¹⁵ Departamento de Física Matemática, Instituto de Física, Universidade de São Paulo, Rua do Matão 1371, CEP 05508-090

¹⁶ Instituto de Astrofísica de Andalucía. IAA-CSIC. Glorieta de la astronomía S/N. 18008, Granada, Spain.

¹⁷ Departamento de Física Teórica e Experimental, Universidade Federal do Rio Grande do Norte, CP 1641, Natal, RN, 59072-970, Brazil

¹⁸ Department of Physics & Astronomy, University of North Carolina at Chapel Hill, NC 27599-3255, USA

¹⁹ Universidade Federal do Paraná, Campus Jandaia do Sul, Rua Dr. João Maximiano, 426, Jandaia do Sul-PR, 86900-000, Brazil

²⁰ Centro Brasileiro de Pesquisas Físicas, Rua Dr. Xavier Sigaud 150, Rio de Janeiro, RJ, CEP 22290-180, Brazil

²¹ Department of Physics, University of Notre Dame, Notre Dame, IN 46556, USA

²² JINA Center for the Evolution of the Elements (JINA-CEE), USA

APPENDIX A: PHOTOMETRIC REDSHIFT PERFORMANCE: TABLES

In Table [A1](#) we present a general overview of the photometric redshift performance as a function of the magnitude, redshift and *Odds*. In Table [A2](#), [A3](#) and [A4](#) this information is extended defining thinner bins in magnitude, redshift and *Odds*, respectively. Finally, we present in Table [A5](#) several *K*-corrections computed with the BPZ2 templates in the *uJAVA* & the *rSDSS* filters.

Table A1. S-PLUS General Table: The table shows the bias (μ_z), the precision (σ_z), and the fraction of outliers (η_z) for all types of galaxies (i.e., *all*), early (i.e., *red*) and late (i.e., *blue*) spectral-types and the fraction of galaxies ($\#$) as a function of the *r*-band magnitude, the redshift and the Odds parameter.

r, z, Odds	μ_z^{all}	σ_z^{all}	η_z^{all}	$\#^{all}$	μ_z^{red}	σ_z^{red}	η_z^{red}	$\#^{red}$	μ_z^{blue}	σ_z^{blue}	η_z^{blue}	$\#^{blue}$
r < 16.0	0.002	0.009	0.004	1	0.001	0.006	0.002	0	0.003	0.013	0.007	0
r < 17.0	0.001	0.011	0.007	6	-0.000	0.009	0.001	2	0.003	0.013	0.013	3
r < 18.0	0.001	0.015	0.008	19	-0.001	0.012	0.002	8	0.003	0.017	0.013	10
r < 19.0	0.002	0.020	0.014	41	-0.001	0.014	0.003	15	0.004	0.024	0.020	25
r < 20.0	0.002	0.026	0.025	69	-0.002	0.019	0.006	25	0.005	0.031	0.037	44
r < 21.0	0.000	0.030	0.036	88	-0.004	0.023	0.010	35	0.004	0.035	0.053	53
z < 0.05	0.015	0.027	0.063	5	0.003	0.010	0.005	1	0.025	0.040	0.080	3
z < 0.10	0.010	0.024	0.039	17	0.002	0.011	0.002	4	0.016	0.031	0.051	13
z < 0.20	0.006	0.025	0.031	44	0.000	0.015	0.002	12	0.010	0.030	0.042	32
z < 0.30	0.004	0.026	0.031	58	-0.000	0.016	0.004	17	0.007	0.031	0.042	41
z < 0.40	0.003	0.026	0.029	69	-0.001	0.018	0.005	23	0.007	0.032	0.041	46
z < 0.50	0.002	0.028	0.028	78	-0.002	0.021	0.006	29	0.005	0.033	0.041	49
z < 1.00	0.000	0.030	0.036	88	-0.004	0.023	0.010	35	0.004	0.035	0.053	53
Odds > 0.00	0.000	0.030	0.036	88	-0.004	0.023	0.010	35	0.004	0.035	0.054	53
Odds > 0.10	0.000	0.029	0.034	86	-0.004	0.023	0.010	35	0.004	0.034	0.050	51
Odds > 0.20	0.000	0.026	0.027	80	-0.004	0.022	0.007	33	0.004	0.030	0.041	46
Odds > 0.30	0.001	0.023	0.023	70	-0.003	0.019	0.005	29	0.004	0.027	0.036	40
Odds > 0.40	0.001	0.020	0.021	57	-0.002	0.016	0.004	24	0.004	0.024	0.034	33
Odds > 0.50	0.001	0.017	0.020	44	-0.001	0.014	0.004	17	0.003	0.020	0.032	26
Odds > 0.60	0.001	0.015	0.019	32	-0.001	0.012	0.003	12	0.003	0.017	0.029	19
Odds > 0.70	0.001	0.013	0.019	23	-0.001	0.010	0.003	9	0.002	0.015	0.029	14
Odds > 0.80	0.001	0.011	0.019	16	-0.000	0.009	0.003	6	0.002	0.013	0.031	9
Odds > 0.90	0.001	0.009	0.020	9	0.000	0.008	0.002	3	0.002	0.010	0.032	5
Odds > 0.95	0.001	0.008	0.017	5	0.001	0.007	0.001	2	0.002	0.009	0.027	3
Odds > 0.99	0.001	0.007	0.009	2	0.001	0.006	0.000	0	0.002	0.008	0.016	1

Table A2. The table shows the bias (μ_z), the precision (σ_z), and the fraction of outliers (η_z) for all types of galaxies (i.e., *all*), early (i.e., *red*) and late (i.e., *blue*) spectral-types and the fraction of galaxies ($\#$) for different magnitude intervals.

r	μ_z^{all}	σ_z^{all}	η_z^{all}	$\#^{all}$	μ_z^{red}	σ_z^{red}	η_z^{red}	$\#^{red}$	μ_z^{blue}	σ_z^{blue}	η_z^{blue}	$\#^{blue}$
14.5 < r < 15.5	0.001	0.008	0.005	0	0.000	0.006	0.003	0	0.003	0.010	0.006	0
15.5 < r < 16.5	0.002	0.010	0.007	2	0.000	0.008	0.001	1	0.003	0.012	0.012	1
16.5 < r < 17.5	0.001	0.014	0.009	7	-0.001	0.012	0.001	3	0.003	0.016	0.015	4
17.5 < r < 18.5	0.001	0.020	0.010	18	-0.002	0.016	0.003	7	0.004	0.024	0.015	11
18.5 < r < 19.5	0.003	0.032	0.029	26	-0.003	0.025	0.007	7	0.007	0.036	0.039	18
19.5 < r < 20.5	-0.003	0.045	0.064	23	-0.011	0.034	0.018	9	0.004	0.054	0.093	14
20.5 < r < 21.5	-0.018	0.047	0.061	16	-0.017	0.038	0.019	10	-0.022	0.076	0.143	5

Table A3. The table shows the bias (μ_z), the precision (σ_z), and the fraction of outliers (η_z) for all types of galaxies (i.e., *all*), early (i.e., *red*) and late (i.e., *blue*) spectral-types and the fraction of galaxies ($\#$) for different redshift intervals.

z	μ_z^{all}	σ_z^{all}	η_z^{all}	$\#^{all}$	μ_z^{red}	σ_z^{red}	η_z^{red}	$\#^{red}$	μ_z^{blue}	σ_z^{blue}	η_z^{blue}	$\#^{blue}$
0.0 < z < 0.1	0.010	0.024	0.041	17	0.003	0.012	0.004	4	0.016	0.031	0.052	13
0.1 < z < 0.2	0.003	0.026	0.026	27	-0.002	0.016	0.003	8	0.007	0.031	0.036	18
0.2 < z < 0.3	-0.002	0.028	0.029	13	-0.002	0.020	0.008	4	-0.002	0.033	0.040	8
0.3 < z < 0.4	-0.002	0.029	0.019	10	-0.003	0.025	0.007	6	-0.000	0.037	0.034	4
0.4 < z < 0.5	-0.017	0.035	0.023	9	-0.016	0.031	0.010	5	-0.022	0.044	0.046	3
0.5 < z < 0.8	-0.032	0.050	0.091	9	-0.023	0.036	0.026	6	-0.075	0.089	0.209	3
0.8 < z < 1.0	-0.206	0.103	0.674	0	-0.199	0.075	0.694	0	-0.223	0.140	0.661	0

Table A4. The table shows the bias (μ_z), the precision (σ_z), and the fraction of outliers (η_z) for all types of galaxies (i.e., *all*), early (i.e., *red*) and late (i.e., *blue*) spectral-types and the fraction of galaxies (#) for different Odds intervals.

Odds	μ_z^{all}	σ_z^{all}	η_z^{all}	$\#^{all}$	μ_z^{red}	σ_z^{red}	η_z^{red}	$\#^{red}$	μ_z^{blue}	σ_z^{blue}	η_z^{blue}	$\#^{blue}$
0.0 < Odds < 0.1	-0.021	0.105	0.159	1	-0.004	0.023	0.010	35	0.004	0.035	0.054	53
0.1 < Odds < 0.2	-0.019	0.087	0.115	6	-0.004	0.023	0.010	35	0.004	0.034	0.050	51
0.2 < Odds < 0.3	-0.008	0.058	0.055	10	-0.004	0.022	0.007	33	0.004	0.030	0.041	46
0.3 < Odds < 0.4	-0.003	0.042	0.031	12	-0.003	0.019	0.005	29	0.004	0.027	0.036	40
0.4 < Odds < 0.5	0.000	0.033	0.025	13	-0.002	0.016	0.004	24	0.004	0.024	0.034	33
0.5 < Odds < 0.6	0.001	0.028	0.025	11	-0.001	0.014	0.004	17	0.003	0.020	0.032	26
0.6 < Odds < 0.7	0.001	0.022	0.019	8	-0.001	0.012	0.003	12	0.003	0.017	0.029	19
0.7 < Odds < 0.8	0.001	0.018	0.017	7	-0.001	0.010	0.003	9	0.002	0.015	0.029	14
0.8 < Odds < 0.9	0.001	0.014	0.019	6	-0.000	0.009	0.003	6	0.002	0.013	0.031	9
0.9 < Odds < 1.0	0.001	0.009	0.020	9	0.000	0.008	0.002	3	0.002	0.010	0.032	5

Table A5. *K*-corrections for the BPZ2 templates utilized in this work, for the *uJAVA* & the *rSDSS* filters. An on-line version of this table (including all filters) is available at the following link: <https://datalab.noao.edu/splus/>

<i>uJAVA</i>	T ₁	T ₂	T ₃	T ₄	T ₅	T ₆	T ₇	T ₈	T ₉	T ₁₀	T ₁₁	T ₁₂	T ₁₃	T ₁₄
0.0 < z < 0.1	0.15	0.16	0.19	0.19	0.21	0.19	0.17	0.16	0.15	0.11	0.12	0.13	0.10	0.07
0.1 < z < 0.2	0.50	0.55	0.58	0.63	0.69	0.64	0.54	0.50	0.46	0.33	0.32	0.19	0.12	0.00
0.2 < z < 0.3	1.04	1.08	1.11	1.20	1.27	1.16	1.00	0.91	0.86	0.68	0.47	0.24	0.13	0.00
0.3 < z < 0.4	1.63	1.69	1.73	1.86	1.93	1.64	1.39	1.26	1.18	0.93	0.66	0.30	0.15	-0.01
0.4 < z < 0.5	2.13	2.25	2.32	2.52	2.56	1.97	1.65	1.49	1.38	1.08	0.88	0.41	0.14	-0.06
0.5 < z < 0.8	2.29	2.47	2.58	2.83	2.83	1.89	1.52	1.36	1.25	0.95	0.91	0.48	0.13	-0.15
0.8 < z < 1.0	3.19	3.52	3.73	4.00	3.56	1.95	1.54	1.36	1.24	0.91	0.99	0.30	0.00	-0.29
1.0 < z < 1.2	3.95	4.43	4.73	4.80	3.82	1.94	1.54	1.35	1.22	0.87	1.22	0.31	-0.01	-0.34
<i>rSDSS</i>	T ₁	T ₂	T ₃	T ₄	T ₅	T ₆	T ₇	T ₈	T ₉	T ₁₀	T ₁₁	T ₁₂	T ₁₃	T ₁₄
0.0 < z < 0.1	0.03	0.03	0.03	0.04	0.04	0.05	0.04	0.04	0.05	0.04	0.05	0.03	0.01	0.01
0.1 < z < 0.2	0.10	0.12	0.12	0.14	0.16	0.19	0.17	0.17	0.17	0.14	0.16	0.08	0.01	-0.04
0.2 < z < 0.3	0.20	0.23	0.24	0.28	0.32	0.36	0.32	0.32	0.32	0.27	0.26	0.12	0.01	-0.09
0.3 < z < 0.4	0.33	0.39	0.41	0.47	0.53	0.57	0.51	0.50	0.48	0.43	0.37	0.15	-0.01	-0.13
0.4 < z < 0.5	0.52	0.60	0.64	0.72	0.79	0.83	0.75	0.72	0.68	0.62	0.51	0.24	0.06	-0.07
0.5 < z < 0.8	1.07	1.20	1.28	1.38	1.48	1.57	1.48	1.39	1.28	1.21	0.95	0.53	0.27	0.06
0.8 < z < 1.0	1.68	1.82	1.93	2.03	2.16	2.25	2.17	2.04	1.89	1.76	1.46	0.95	0.62	0.29
1.0 < z < 1.2	2.12	2.28	2.41	2.54	2.71	2.75	2.60	2.43	2.26	2.04	1.68	1.01	0.63	0.24